International Journal of Heat and Mass Transfer 141 (2019) 327–345

Contents lists available at ScienceDirect

International Journal of Heat and Mass Transfer

journal homepage: www.elsevier.com/locate/ijhmt

Oscillatory instability of a 3D natural convection flow around a tandem of cold and hot vertically aligned cylinders placed inside a cold cubic enclosure

Avihai Spizzichino [a,b], Efi Zemach [b], Yuri Feldman [a,*]

[a] Department of Mechanical Engineering, Ben-Gurion University of the Negev, P.O. Box 653, Beer-Sheva 84105, Israel
[b] Soreq NRC, Yavne 81800, Israel

ARTICLE INFO

Article history:
Received 6 November 2018
Received in revised form 12 June 2019
Accepted 13 June 2019

Keywords:
Oscillatory instability
Reflectional symmetry breaking
Hopf bifurcation
Supercritical flow

ABSTRACT

The oscillatory instability of a 3D natural convection flow in a cold cubic enclosure containing a tandem of cold and hot vertically aligned cylinders is investigated in detail as a function of the distance between the cylinders. The study is performed by applying time integration of slightly supercritical flows. The flows undergo a transition to unsteadiness via either reflectional symmetry breaking or reflectional symmetry preserving Hopf bifurcation as a function of the distance between the cylinders. An extensive discussion of the observed instability scenarios is presented, and the different instability mechanisms are characterized in terms of the values of the main oscillating harmonics and the spatial distribution of the oscillating amplitudes of all the fields obtained for slightly supercritical flows.

1. Introduction

Natural convection flow in a confined rectangular container is a basic heat transfer mechanism, which is characterized by spontaneous mass transfer of the working fluid, dominated by the action of buoyancy forces. The forces result from a non-uniform temperature distribution of the fluid in the presence of a gravity field, which can be achieved by heating the cavity walls (for example, Rayleigh-Bernard or differentially heated cavity configurations) or by embedding discrete thermally active sources (or sinks) into the bulk flow. The thermal sources can either be mounted flush on the walls (see e.g. [1–4]) or take the form of discrete thermally active bodies of various shapes immersed in the bulk of the convective flow. Various setups of the latter configuration have been the focus of extensive theoretical and experimental research in the past two decades, as they comprise convenient test beds for versatile engineering applications, including heat exchangers filled with nanofluids [5–8], nuclear and chemical reactors [9,10], cooling systems for electronics [11–13] and energy storage systems [14,15].

Positioned inside the enclosure, the discrete thermally active sources not only drive the flow, but also substantially affect the characteristics of the flow regime as a result of the imposition of no-slip kinematic constraints on all the source surfaces. Among all possible geometries, cylindrically shaped heat sources have attracted much of the attention in the literature, due both to their particular relevance to many of the above-mentioned engineering applications and to their purely theoretical interest. The theoretical research in this area focuses on both 2D and 3D configurations consisting of a single hot cylinder positioned inside a rectangular enclosure with either cold or locally heated walls. With regard to 2D geometries, the following studies are worthy of mention: Hussain and Hussein [16] investigated the flow around an isoflux circular cylinder at different vertical locations and different values of the Rayleigh number (Ra); Lee et al. [17] studied different regimes of convective flow around a centrally placed hot cylinder as a function of the Ra value and the size of the local heating zone attached to the bottom cavity wall; Park et al. [18,19] and Seo et al. [20,21] investigated natural convection flow in the presence of up to four hot cylinders with varying horizontal and vertical orientations for the range of $10^3 \leqslant Ra \leq 10^6$; Hussain and Rahomey [22] recently described natural convection in the presence of cylinders of different geometries inside a square enclosure filled with porous layers superposed with a nanofluid; and Feldman [23] investigated the oscillatory instability of natural convection flow in the presence of a tandem of vertically aligned cylinders.

The results obtained from the simulation of 2D flows imply zero velocity and pressure gradients in the spanwise direction and should therefore be interpreted with care. To completely characterize instabilities of natural convection flow in realistic geometries characterized by a finite size in the spanwise direction, fully

* Corresponding author.
E-mail address: yurifeld@bgu.ac.il (Y. Feldman).

https://doi.org/10.1016/j.ijheatmasstransfer.2019.06.050
0017-9310/

3D simulations should be performed. As a result of the high computational costs and the non-trivial spatial discretization, the state-of-the-art research addressing natural convection flow in 3D containers containing embedded cylindrical heat sources is quite sparse. Nonetheless, ever increasing computational power, has facilitated some research, mostly in the past decade, and this work can be logically divided into applied and basic theoretical studies. Among the applied studies, worthy of mention are works introducing the concept of smart thermo-insulating materials [24,25]. Basic theoretical research has focused mainly on addressing the 3D instability of natural convection flow in rectangular geometries in the presence of a single hot cylinder placed inside a cold cubic cavity [26] or an array of horizontally oriented hot cylinders in a periodic rectangular channel [27]. Another area of research interest has centered on the investigation of the 3D flow effects in a horizontal enclosure with an embedded adiabatic body [28,29] by applying periodic boundary conditions in the spanwise direction.

The present research aims to investigate the characteristics of 3D instability inherent in natural convection flow in a cubic cavity, with all no-slip boundaries, in the presence of a tandem of vertically aligned horizontal hot and cold cylinders. Investigations of this type of flow belong to the family of the most general TriGlobal studies, i.e., analysis of global instability in a 3D domain with three inhomogeneous spatial directions [30]. For many years, the investigation of 3D instabilities of this type was considered challenging, if not unfeasible. Nowadays, however, with the increase of available computational power and the development of advanced numerical techniques, this analysis has become trivial for 2D flow configurations and possible for some 3D flow configurations [30]. In particular, the present study is performed by applying a recently developed and thoroughly verified methodology comprising the semi-implicit direct forcing immersed boundary (IB) method based on the Schur complement approach [31].

Following the recent works of [32,33], the problem is addressed by analyzing the time evolution of slightly supercritical flows obtained by direct numerical simulation (DNS). The key idea is to perform time integration of the flow for a time interval that is sufficiently long to preserve only the single most unstable (leading) eigenmode, while the impact of all the other eigenmodes is either totally suppressed or kept sufficiently small. To ensure high accuracy, it is critical to fully resolve all flow scales, which limits the analysis to configurations undergoing steady-unsteady transitions at relatively moderate Ra values. A tandem of vertically aligned horizontal hot and cold cylinders confined by a cold cubic cavity and shifted downwards and upwards relative to the cavity center, respectively, ideally meets the above limitation, as it generates natural convection flow undergoing a steady-unsteady transition as small at a Ra of $\sim O\left(10^5\right)$. Despite the very simple geometric setup, the above alignment gives rise to the formation of fully 3D, highly separated, thermally driven flows, which exhibit a number of yet to be revealed scenarios of oscillatory instability varying as a function of the distance between the cylinders. Characterization of the above instabilities is of considerable fundamental interest and is the focus of the present study. The investigation includes elucidation of the symmetry breaking and symmetry preserving phenomena and characterization of the spatial distribution of the vortical structures and the leading eigenvector inherent in the supercritical flow, which together shed light on the physical mechanisms responsible for the instability onset typical of the above configurations.

2. Theoretical background

A tandem of cold and hot cylinders of diameter D aligned along the vertical centerline of a cubic enclosure of side L (see Fig. 1) is considered. The enclosure is filled with air and is subjected to a gravitational field acting in the direction negative to the z axis. The upper cold cylinder and the lower hot cylinder are held at constant temperatures T_c and T_h, respectively, and the distance between the cylinders is equal to δ. The front and rear walls of the cavity are thermally insulated, while all the other walls are held at constant temperature T_c, as shown in Fig. 1. The ratio between the cylinder diameter, D, and the length of the cavity side, L, is fixed at $D/L = 0.2$. The dynamics of the fluid can be described by the incompressible continuity, Navier Stokes (NS) and energy equations (Eqs. (1)–(3)):

$$\nabla \cdot \boldsymbol{u} = 0, \tag{1}$$

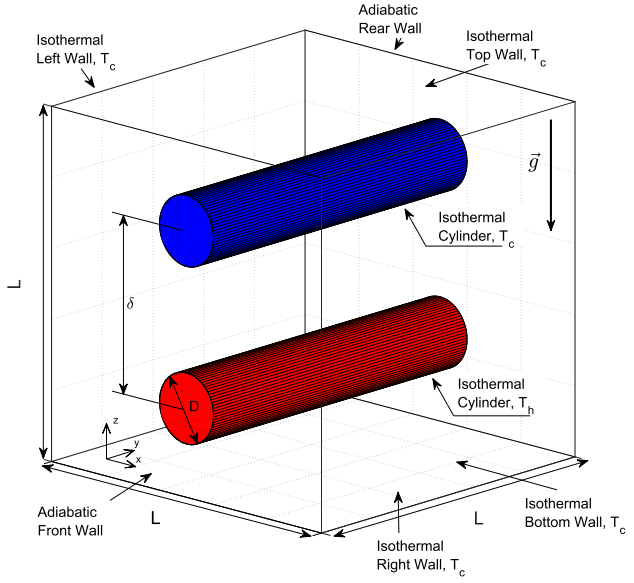

Fig. 1. Physical model of a tandem of horizontal cold and hot cylinders vertically aligned inside a cold cube.

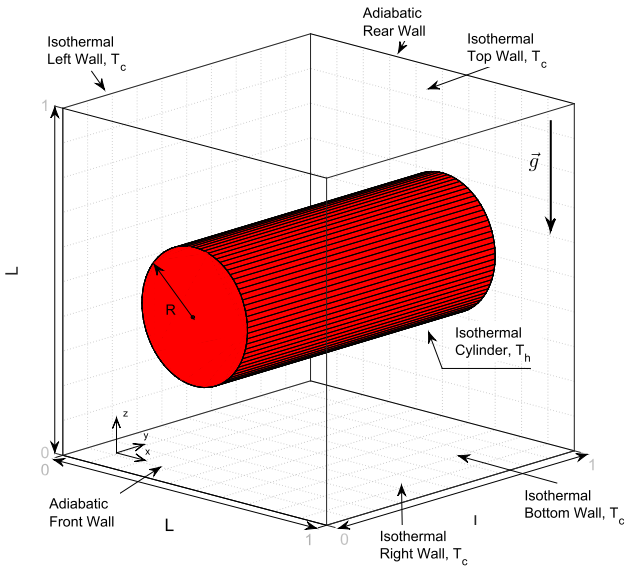

Fig. 2. Physical model of a hot cylinder of radius R placed inside a cold cube and aligned along its horizontal centerline.

Table 1
Comparison between the present study and the previously published values [26] (as measured by photogrammetry of the corresponding charts) for $\overline{Nu}$,averaged over the surface of a hot cylinder placed within a cold cube and $\overline{Nu}_G$, averaged over the surface of the cold cube.

	$Ra = 10^4$				$Ra = 10^5$				$Ra = 10^6$			
	Nu		Nu_G		Nu		Nu_G		Nu		Nu_G	
R/L	Ref. [26]	Present	Ref. [26]	Present	Ref. [26]	Present	Ref. [26]	Present	Ref. [26]	Present	Ref. [26]	Present
0.1	6.2493	6.4880	1.0201	1.0208	11.138	11.662	1.8099	1.8360	18.3260	19.2500	2.9945	3.0348
0.2	5.1184	5.1500	1.6161	1.6188	7.2271	7.5800	2.3766	2.3814	13.3610	13.9370	4.3985	4.3677
0.3	5.8084	5.7304	2.6216	2.9091	6.4790	6.5169	2.9726	3.0702	11.2720	11.4010	5.1956	5.3844
0.4	8.7030	8.5544	5.1919	5.3928	8.7030	8.7643	5.2651	5.5131	10.7160	10.8320	6.6106	6.8313

Table 2
Coordinates of points at which the temperature evolution was acquired.

Point number	X	Y	Z
P1	0.25	0.4875	0.25
P2	0.25	0.4875	0.75
P3	0.75	0.4875	0.25
P4	0.75	0.4875	0.75
P5	0.25	0.5125	0.25
P6	0.25	0.5125	0.75
P7	0.75	0.5125	0.25
P8	0.75	0.5125	0.75

Table 3
Maximal and minimal values of the Nusselt numbers $\overline{Nu}_c$ and $\overline{Nu}_h$, averaged over the surfaces of the cold and hot cylinders, respectively, along with the value of ω corresponding to the angular frequency of the leading harmonics as a function of δ. The calculations were performed on 200^3 and 300^3 uniform structured grids.

	$max\ (\overline{Nu}_c)$		$min\ (\overline{Nu}_c)$		$max\ (\overline{Nu}_h)$		$min\ (\overline{Nu}_h)$		ω	
δ/Grid	200^3	300^3	200^3	300^3	200^3	300^3	200^3	300^3	200^3	300^3
0.4	−0.846	−0.837	−1.517	−1.530	13.824	13.871	13.428	13.460	0.348	0.347
0.5	−0.895	−0.891	−1.017	−1.017	14.127	14.162	13.981	14.013	0.815	0.815
0.6	−0.984	−0.987	−1.642	−1.640	16.645	16.678	16.267	16.480	0.945	0.945

Table 4
Maximal and minimal values of the temperature θ monitored at control points P. 2, P. 3 and P. 4 (see Table 2) as a function of δ. The calculations were performed on 200^3 and 300^3 uniform structured grids.

	$\delta = 0.4$				$\delta = 0.5$				$\delta = 0.6$			
	θ_{max}, P.3		θ_{min}, P.3		θ_{max}, P.4		θ_{min}, P.4		θ_{max}, P.2		θ_{min}, P.2	
Grid	200^3	300^3	200^3	300^3	200^3	300^3	200^3	300^3	200^3	300^3	200^3	300^3
	0.157	0.156	0.131	0.129	0.297	0.298	0.284	0.284	0.278	0.280	0.226	0.228

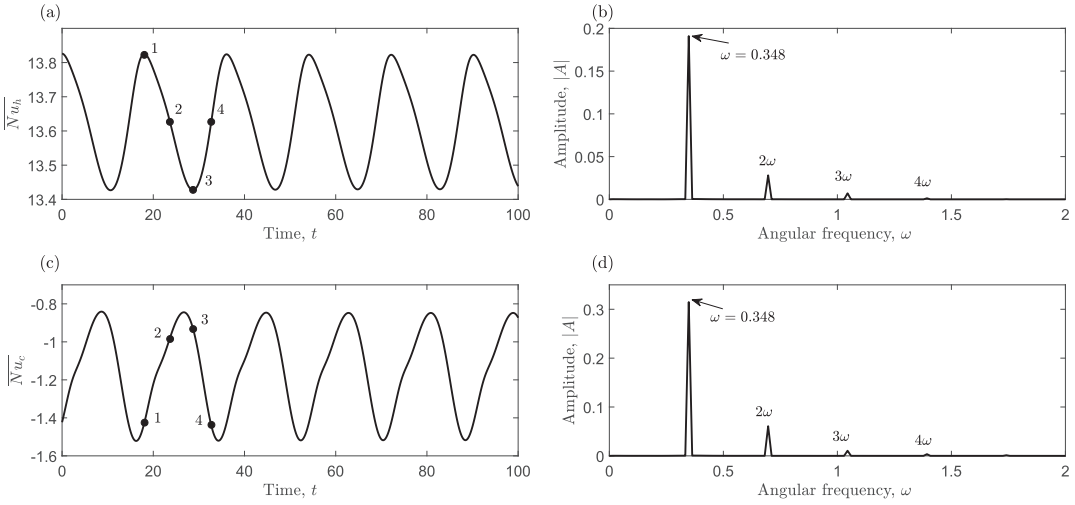

Fig. 3. Time evolution of the averaged $\overline{Nu}_h$ and $\overline{Nu}_c$ numbers and the corresponding Fourier spectra obtained for the values of $\delta = 0.4, Ra = 2 \times 10^5$. The results were obtained on a 200^3 structured uniform grid.

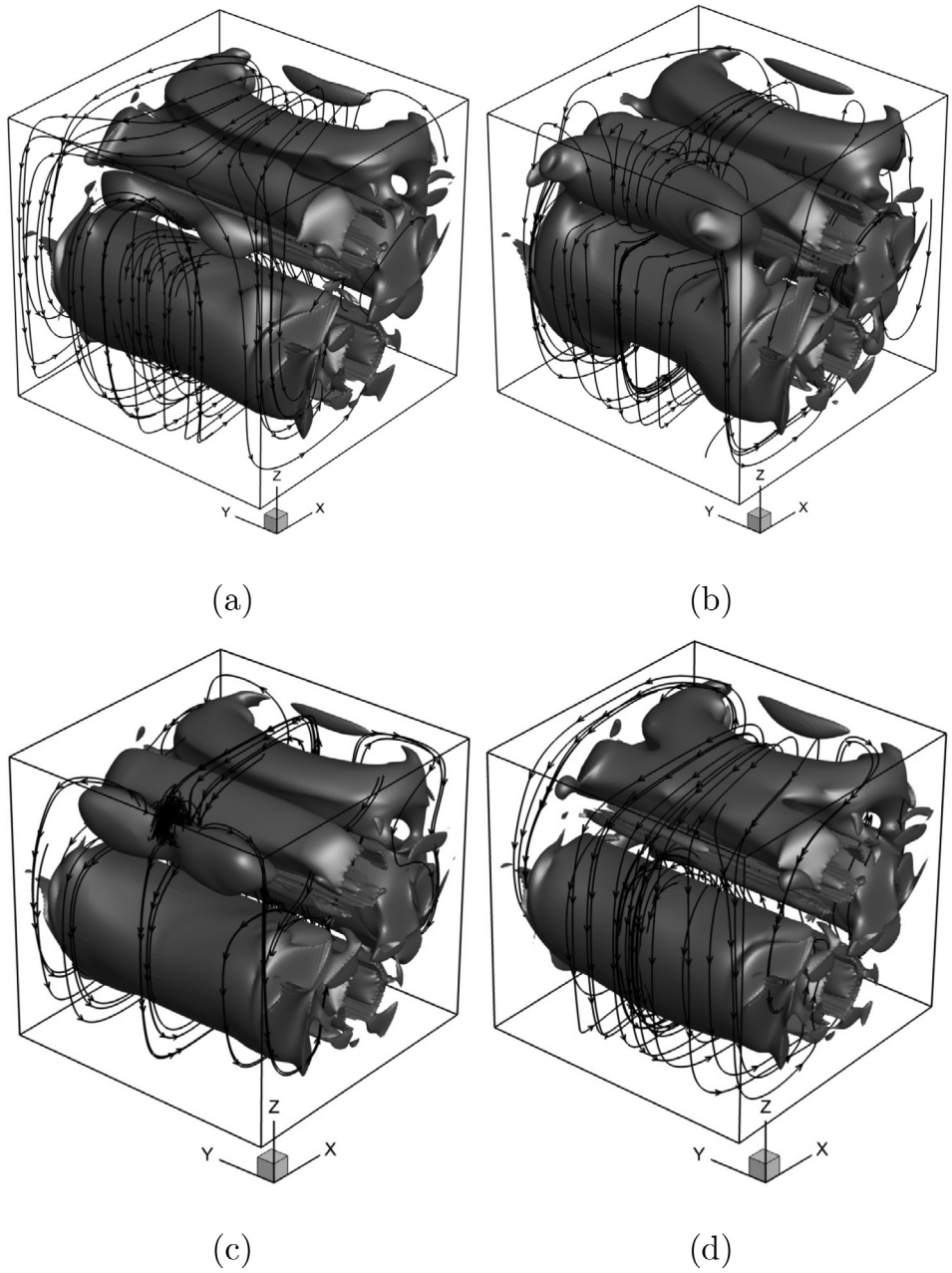

Fig. 4. Snapshots of the spatial distribution of the isosurfaces of $\lambda_2 = -0.1$ superimposed by stream traces shown at four representative instances taken evenly throughout an oscillation period: 1 (a); 2 (b); 3(c); 4(d). The time instances 1–4 are defined in Fig. 3, $\delta = 0.4, Ra = 2 \times 10^5$. The results were obtained on a 200^3 structured uniform grid.

$$\frac{\partial \boldsymbol{u}}{\partial t} + (\boldsymbol{u} \cdot \nabla)\boldsymbol{u} = -\nabla p + \sqrt{\frac{Pr}{Ra}}\nabla^2 \boldsymbol{u} + \theta \vec{e}_z + \boldsymbol{f}, \tag{2}$$

$$\frac{\partial \theta}{\partial t} + (\boldsymbol{u} \cdot \nabla)\theta = \frac{1}{\sqrt{PrRa}}\nabla^2 \theta + q, \tag{3}$$

where $\boldsymbol{u} = (u, v, w), p, t$ and θ are the non-dimensional velocity, pressure, time and temperature, respectively, and $\vec{e}_z$ is a unit vector in the direction opposite to that of the gravity force. The flow buoyancy effects are addressed by applying the Boussinesq approximation, $\rho = \rho_0(1 - \beta(T - T_c))$[1], which results in the appearance of an additional temperature term as a source in the momentum equation in the z direction and makes it possible to couple the temperature and the velocity. The volumetric forces $\boldsymbol{f}$ and the heat fluxes q appearing as sources in Eqs. (2) and (3) are additional unknowns introduced to express the influence of the immersed cylinders on the momentum and energy conservation of the flow. The problem is scaled by $L, U = \sqrt{g\beta L \Delta T}, t = L/U$, and $P = \rho U^2$ for length, velocity, time and pressure, respectively, where ρ is the mass density of the working fluid, g is the gravitational acceleration, β is the isobaric coefficient of thermal expansion, and $\Delta T = T_h - T_c$ is the temperature difference between the hot and cold cylinders. The non-dimensional temperature θ is defined as $\theta = (T - T_c)/\Delta T$. The Ra and Prandtl (Pr) numbers are $Ra = \frac{g\beta}{\nu\alpha}\Delta T L^3$ and $Pr = \nu/\alpha$, where ν is the kinematic viscosity and α is the thermal diffusivity. The value of $Pr = 0.71$, corresponding to air, is used in all the numerical simulations performed within the framework of the present study.

[1] Here ρ_0 is the reference density of the liquid at $T = T_c$.

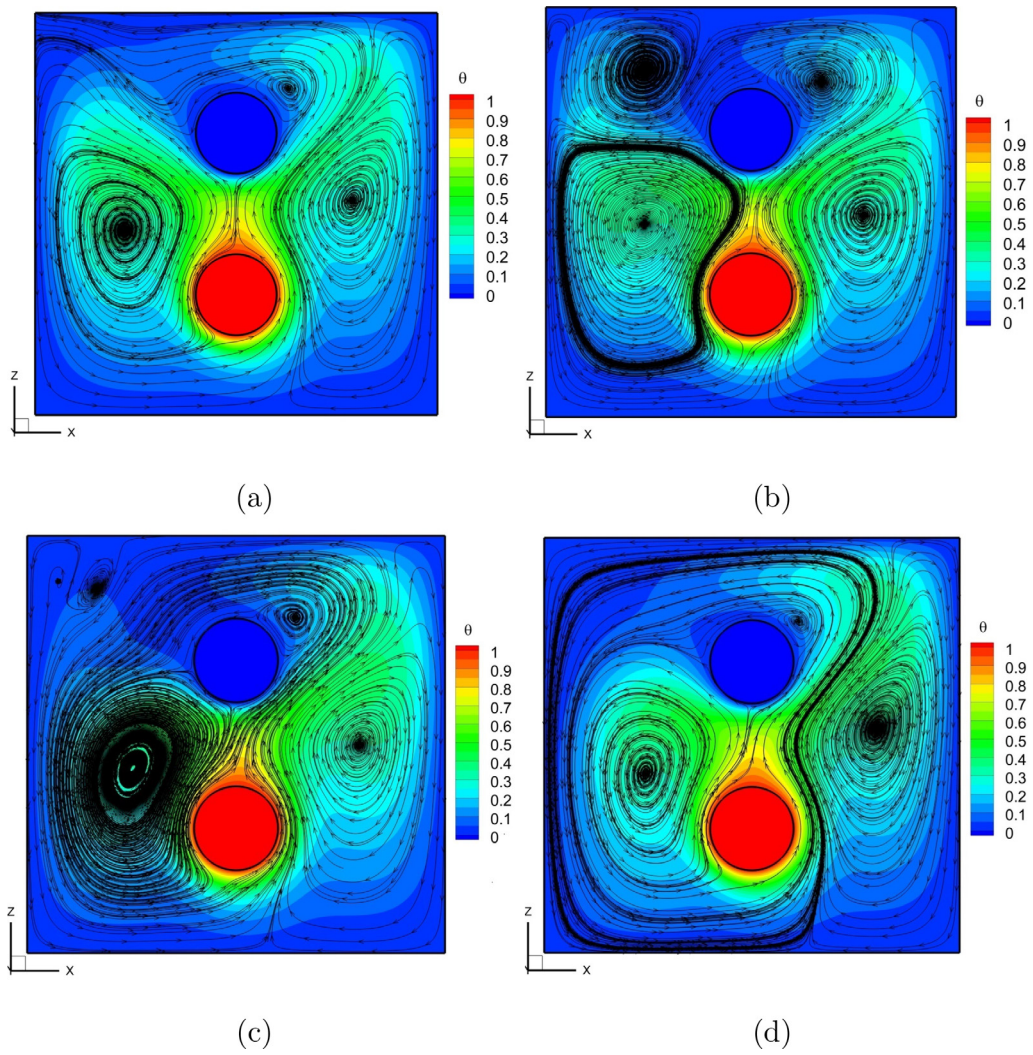

Fig. 5. Snapshots of the spatial temperature distributions at the central cross section $(X-Z)$ shown at four representative instances taken evenly throughout an oscillation period: 1 (a); 2 (b); 3(c); 4(d). The time instances 1–4 are defined in Fig. 3, $\delta = 0.4, Ra = 2 \times 10^5$. The results were obtained on a 200^3 structured uniform grid.

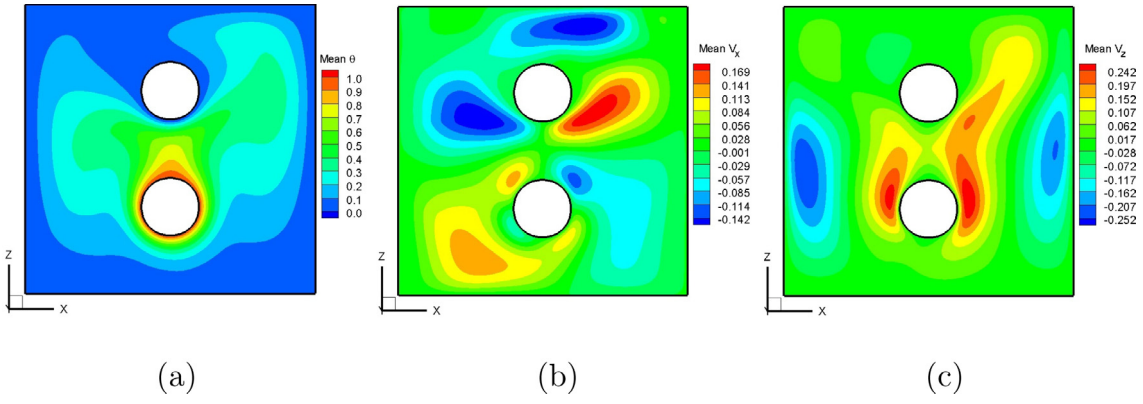

Fig. 6. Distribution of the mean flow characteristics obtained in the midplane $(X-Z)$ for: (a) temperature θ; (b) mean v_x velocity component; (c) mean v_z velocity component, $\delta = 0.4, Ra = 2 \times 10^5$. The results were obtained on a 200^3 structured uniform grid.

Eqs. (1)–(3) are solved by utilizing the semi-implicit direct forcing IB method recently developed in [31]. For the sake of completeness, a brief description of the method follows. According to the IB method formalism, the surface of the immersed body is determined by a set of discrete Lagrangian points, whose location does not necessarily coincide with the underlying Eulerian grid. It is important to note that the distance between the neighboring points of the immersed body surface, Δl, and the width of an Eulerian grid cell, Δx, should be approximately the same. For this reason, a uniform structured grid is used for discretization of the

cubic cavity. To facilitate exchange of information between the Euelerian and the Lagrangian grids, the interpolation operator $\boldsymbol{I}$ and the regualarization operator $\boldsymbol{R}$ are defined as follows:

$$\boldsymbol{R}\left(\boldsymbol{F}^k\left(\boldsymbol{X}^k\right), Q^k\left(\boldsymbol{X}^k\right)\right) = \int_S \left(\boldsymbol{F}^k\left(\boldsymbol{X}^k\right), Q^k\left(\boldsymbol{X}^k\right)\right) \cdot d\left(\boldsymbol{x}_i - \boldsymbol{X}^k\right) dV_S^k, \quad (4a)$$

$$\boldsymbol{I}(\boldsymbol{u}(\boldsymbol{x}_i), \theta(\boldsymbol{x}_i)) = \int_\Omega (\boldsymbol{u}(\boldsymbol{x}_i), \theta(\boldsymbol{x}_i)) \cdot d\left(\boldsymbol{X}^k - \boldsymbol{x}_i\right) dV_{\Omega_i}. \quad (4b)$$

The interpolation operator $\boldsymbol{I}$ interpolates the values of the Eulerian velocities $\boldsymbol{u}(\boldsymbol{x}_i)$ and temperatures $\theta(\boldsymbol{x}_i)$ to the nearby Lagrangian points $\boldsymbol{X}^k$, while an adjoint regularization operator $\boldsymbol{R}$ smears the values of the Lagrangian volumetric force $\boldsymbol{F}^k\left(\boldsymbol{X}^k\right)$ and the heat flux $Q^k\left(\boldsymbol{X}^k\right)$ to the nearby Eulerian grid. Here, S corresponds to all the cells belonging to the immersed body surface, Ω corresponds to a group of flow domain cells located in the close vicinity of the immersed body surface, dV_S^k corresponds to the virtual volume surrounding each Lagrangian point k, and dV_{Ω_i} is the volume of the corresponding cell of the Eulerian flow domain, whose velocity and temperature values are involved in enforcing the boundary conditions at point k of the immersed body. Both interpolation and regularization operators use convolutions with the same discrete Dirac delta function d of the form:

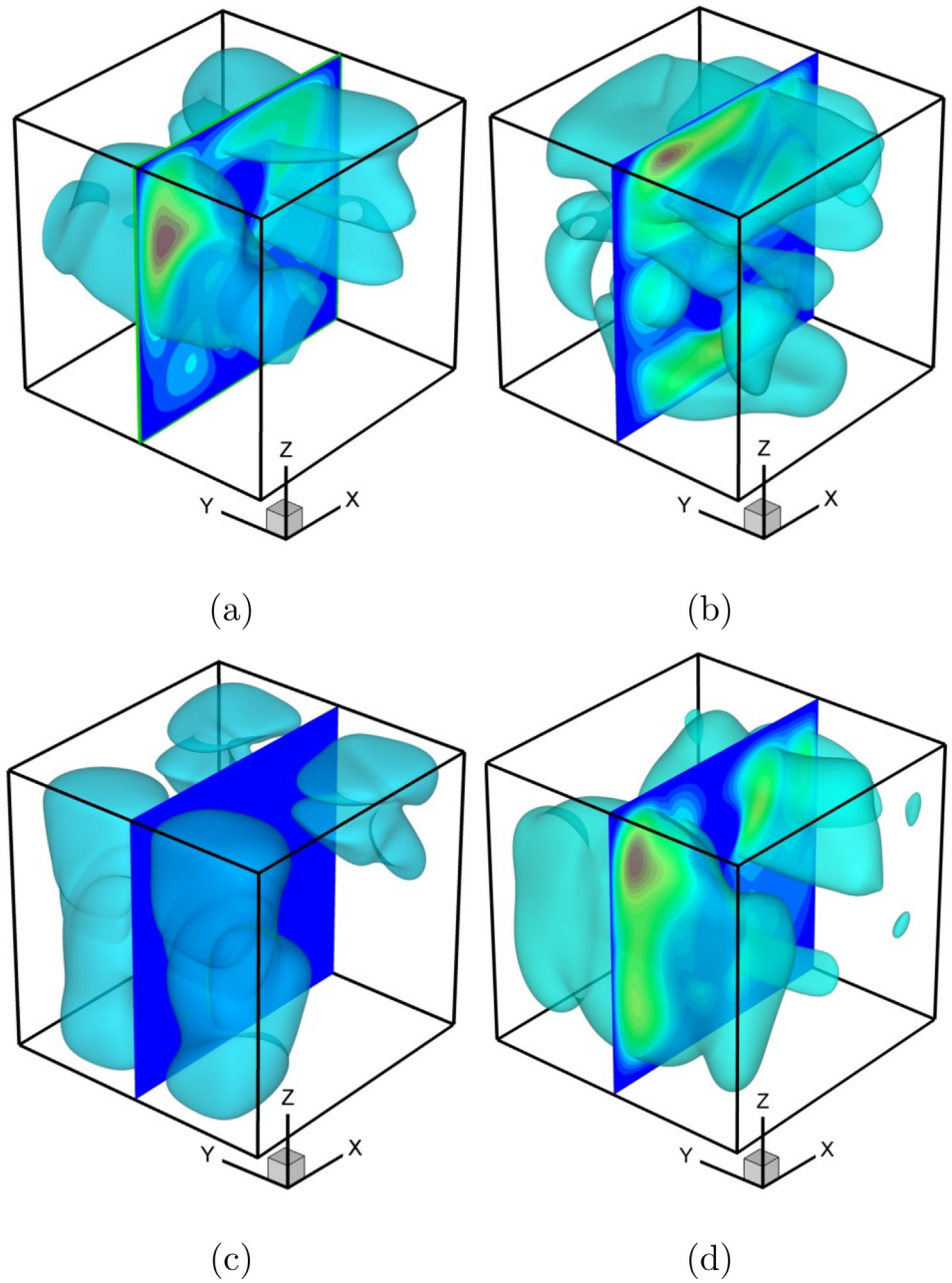

Fig. 7. Isosurfaces of the oscillation amplitudes obtained for: (a) temperature, θ; (b) u_x velocity component; (c) u_y velocity component; and (d) u_z velocity component. The isosurfaces confine the regions characterized by at least 25% of the absolute maximum value. Colors correspond to the relative intensities of the oscillations, $\delta = 0.4, Ra = 2 \times 10^5$. The results were obtained on a 200^3 structured uniform grid.

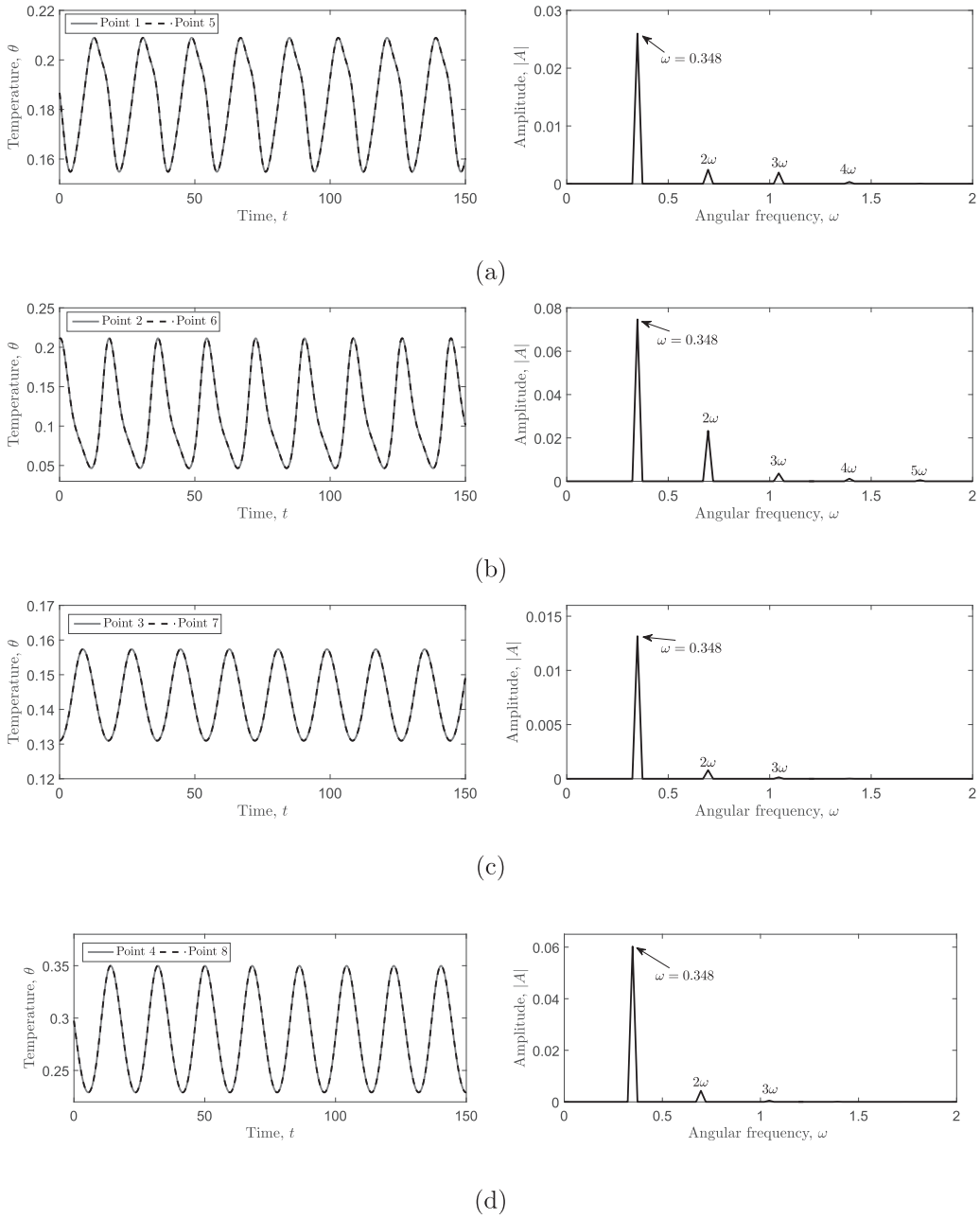

Fig. 8. Temperature monitored at eight points symmetrically distanced relative to the $(X-Z)$ midplane for $\delta = 0.4, Ra = 2 \times 10^5$: (a) time evolution; and (b) Fourier spectrum. The results were obtained on a 200^3 structured uniform grid.

$$d(r) = \begin{cases} \frac{1}{6\Delta r}\left[5 - 3\frac{|r|}{\Delta r} - \sqrt{-3\left(1-\frac{|r|}{\Delta r}\right)^2 + 1}\right] & \text{for } 0.5\Delta r \leqslant |r| \leqslant 1.5\Delta r, \\ \frac{1}{3\Delta r}\left[1 + \sqrt{-3\left(\frac{|r|}{\Delta r}\right)^2 + 1}\right] & \text{for } |r| \leqslant 0.5\Delta r, \\ 0 & \text{otherwise}, \end{cases} \tag{5}$$

introduced by Roma et al. in [34] and verified in a number of studies [31,35–38]. Here, Δr is the cell width in the r direction. Closure of the system of Eqs. (1)–(3) is achieved by introducing kinematic constraints:

$$\boldsymbol{U}_b(\boldsymbol{X}_k) = \boldsymbol{I}(\boldsymbol{u}(\boldsymbol{x})), \tag{6}$$

$$\Theta_b(\boldsymbol{X}_k) = \boldsymbol{I}(\theta(\boldsymbol{x})), \tag{7}$$

to enforce the no-slip boundary condition for all velocity components and the given temperature values[2] on the cylinder surfaces. The continuity, NS, and energy Eqs. (1)–(3) are discretized by using a second-order backward finite difference scheme for the time discretization and a second-order conservative finite volume method implemented on a staggered uniform structured grid for the spatial discretization. All the linear terms are treated implicitly, while all the non-linear terms are taken explicitly from the previous time step and are put into the right hand side of the equations. The system of Eqs. (1)–(3), (6), (7)) is solved by employing the semi-implicit direct forcing IB method [31]. The method exploits the SIMPLE approach

[2] Here $\boldsymbol{U}_b$ and Θ_b are the values of velocity and temperature, respectively, on the surface of each cylinder. In the present study $\boldsymbol{U}_b$=0 on the surface of each cylinder, while $\Theta_b = 1$ on the surface of the hot cylinder and $\Theta_b = 0$ on the surface of the cold cylinder.

for the pressure–velocity coupling, while every component of the non-solenoidal velocity is implicitly coupled with the values of $\boldsymbol{f}$ and q by utilizing the Schur complement approach. Note that at this point the Lagrangian kinematic constraints $\boldsymbol{F}^k$ and Q^k related by Eqs. (4a) and (4b) to the corresponding Eulerian terms $\boldsymbol{f}$ and q are calculated along with the still non-solenoidal velocity field. The obtained non-solenoidal velocity field is then projected to the divergence-free subspace by a standard projection-correction step. For further details regarding implementation details, including an extensive verification study of the applied approach, Ref. [31] should be consulted.

The Nusselt number, Nu, is defined as the ratio of convective to conductive heat fluxes from the given surface, which in accordance with [31] facilitates the calculation of its average value for the surface of each cylinder by:

$$\overline{Nu} = \sqrt{PrRa}\Delta x\overline{Q}, \tag{8}$$

where the average heat flux $\overline{Q}$ is the arithmetic mean of all the non-dimensional heat fluxes Q_k at each Lagrangian point k of the immersed surface, intrinsically calculated by the solution of the system of Eqs. (1)–(3), (6), (7). An additional quantity that will be further used for the verification purposes is the average value of the global Nusselt number $\overline{Nu}_G$, which expresses the global heat flux through the surface of the confining cubic enclosure and is defined as:

$$\overline{Nu}_G = \frac{1}{N}\sum_{i=1}^{N}\overline{\frac{\partial\theta}{\partial\boldsymbol{n}}}, \tag{9}$$

where N corresponds to a number of thermally un-insulated edges and $\overline{\frac{\partial\theta}{\partial\boldsymbol{n}}}$ is the temperature gradient averaged over the surface of a given edge of the cube.

3. Verification study

To verify the numerical method utilized in the present study, a configuration consisting of a single hot cylinder aligned along the horizontal centerline of a cold cube (See Fig. 2) was analyzed, and the obtained flow characteristics were compared with the available data [26] in terms of the values of the Nusselt number, $\overline{Nu}$, averaged over the surface of the hot cylinder, and the values of the global Nusselt number, $\overline{Nu}_G$, averaged over all the surfaces of the cubic enclosure. All the simulations were performed on a 200^3 uniform structured grid with a time step equal to $\Delta t = 10^{-3}$. No-slip boundary conditions were set on all the walls of the cubic enclosure and on the surface of the cylinder. The cylinder's surface was held at a constant hot temperature T_h, and the front and rear walls of the cubic enclosure were adiabatic, while all other walls of the cubic enclosure were held at a constant cold temperature, T_c, as shown in Fig. 2. The results obtained for values of $Ra = 10^3, 10^4$ and 10^5 and values of $R/L = 0.1, 0.2$ and 0.3 were compared with the corresponding independent data [26], as shown in Table 1. Acceptable agreement was observed between the current and the previously reported values of $\overline{Nu}$ and $\overline{Nu}_G$ for the entire range of Ra and R/L, a finding that verifies the applied numerical methodology. Remarkably, in contrast to [26], which reported quasiperiodic and periodic flows for $R/L = 0.3$ and $R/L = 0.4$, respectively, at $Ra = 10^6$, our simulations gave steady-state flows for the entire range of R/L and Ra values. This difference may be attributed to the non-linear physics of the system, which at the same value of the Ra number can sustain a number of different states, as was extensively discussed in a recent study [31]. This argument is supported by grid and time-step independence studies, a detailed comparison of the isosurfaces of the temperature field, and a comparison of the structures of convection cells [31] and is not repeated here for the sake of conciseness.

4. Results and discussion

Numerical simulations were performed for three different configurations with values of $\delta = 0.4, 0.5$ and 0.6. For each configuration, the supercritical regime was found by successively increasing the Ra value by about 10% and taking the values of all the previously obtained flow fields as the initial condition until the steady-unsteady transition of the developed natural convection flow was detected. The transition was detected by monitoring the time evolution of both $\overline{Nu}_h$ and $\overline{Nu}_c$ averaged over the surfaces of the hot and cold cylinders, respectively. After the transition was detected, we verified that the time evolutions of both $\overline{Nu}_h$ and $\overline{Nu}_c$ were governed by single oscillating harmonics, corresponding to the oscillating frequency of the leading eigenmode, while the impact of the other stable eigenmodes was suppressed as a result of a sufficiently long time integration. This argument is based on

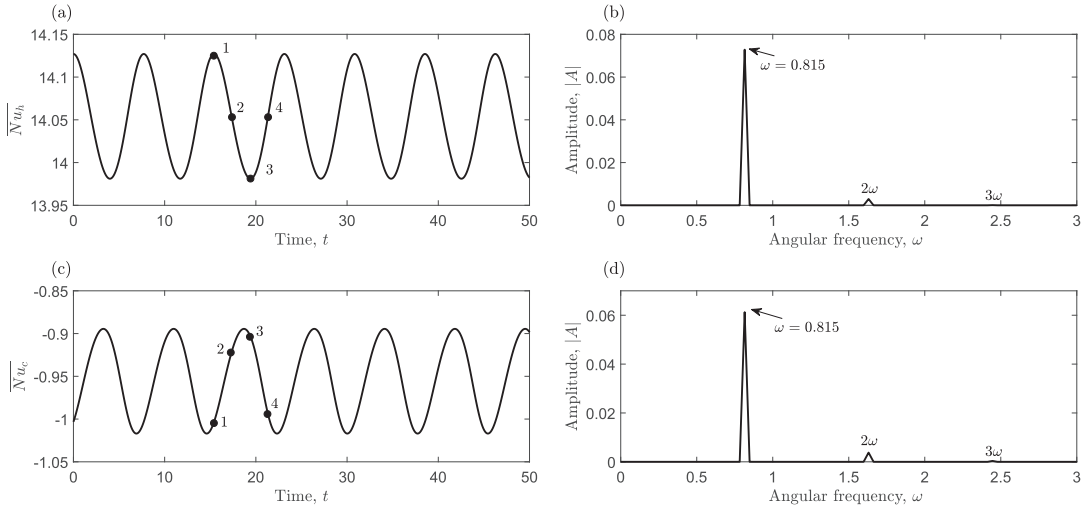

Fig. 9. Time evolution of the averaged $\overline{Nu}_h$ and $\overline{Nu}_c$ numbers and the corresponding Fourier spectra obtained for the values $\delta = 0.5, Ra = 2 \times 10^5$. The results were obtained on a 200^3 structured uniform grid.

the Hopf theorem, which can be described in the vicinity of the bifurcation point as [39]:

$$\phi(t, Ra) = \phi(Ra_{cr}) + \varepsilon Real\left(\Phi e^{i\omega t}\right) + O\left(\varepsilon^2\right), \quad (10)$$

where $\phi(Ra_{cr})$ is the steady-state of any flow characteristic at the critical point and $\mathbf{\Phi}$ is the eigenvector of the corresponding flow characteristic whose eigenvalue is given by $\lambda = i\omega_{cr}$. Although an explicit determination of critical Ra values is beyond the scope of the present study, we note in passing that all the simulations presented in the current study were performed for Ra values not exceeding the corresponding critical Ra_{cr} values by more than 10%, thus ensuring that the analysis was performed for slightly supercritical flows. It should be noted that although the averaged $\overline{Nu}_h$ and $\overline{Nu}_c$ numbers comprise a convenient parameter for determination of the steady-unsteady transition, both parameters are processed, rather than primitive flow variables which in some cases can lead to misinterpretation of the realistic transition phenomenon [23]. For this reason, the description of all the transition regimes reported in the present study was further supported by the analysis of temperature evolution acquired for a number of control points.

In accordance with all the above considerations, the analysis was performed for the values of $Ra = 2 \times 10^5$ for the first two configurations ($\delta = 0.4$ and 0.5) and for the value of $Ra = 3.4 \times 10^5$ for the third configuration ($\delta = 0.6$), resulting in the development of a slightly supercritical flow regime in each configuration. The instabilities observed for each flow configuration were characterized in terms of: the time histories of the Nusselt numbers, $\overline{Nu}_h$ and $\overline{Nu}_c$, averaged over the surfaces of the hot and cold cylinders, respectively; the isosurfaces of $\lambda_2 = -0.1$, whose negative and close-to-zero value determines the outermost outer surface of the vortical structures [40]; the mean fields calculated for every flow characteristics; the isosurfaces of the oscillation amplitudes for all the flow fields, which for slightly supercritical flows exhibit a strong qualitative similarity to the structure of the corresponding leading

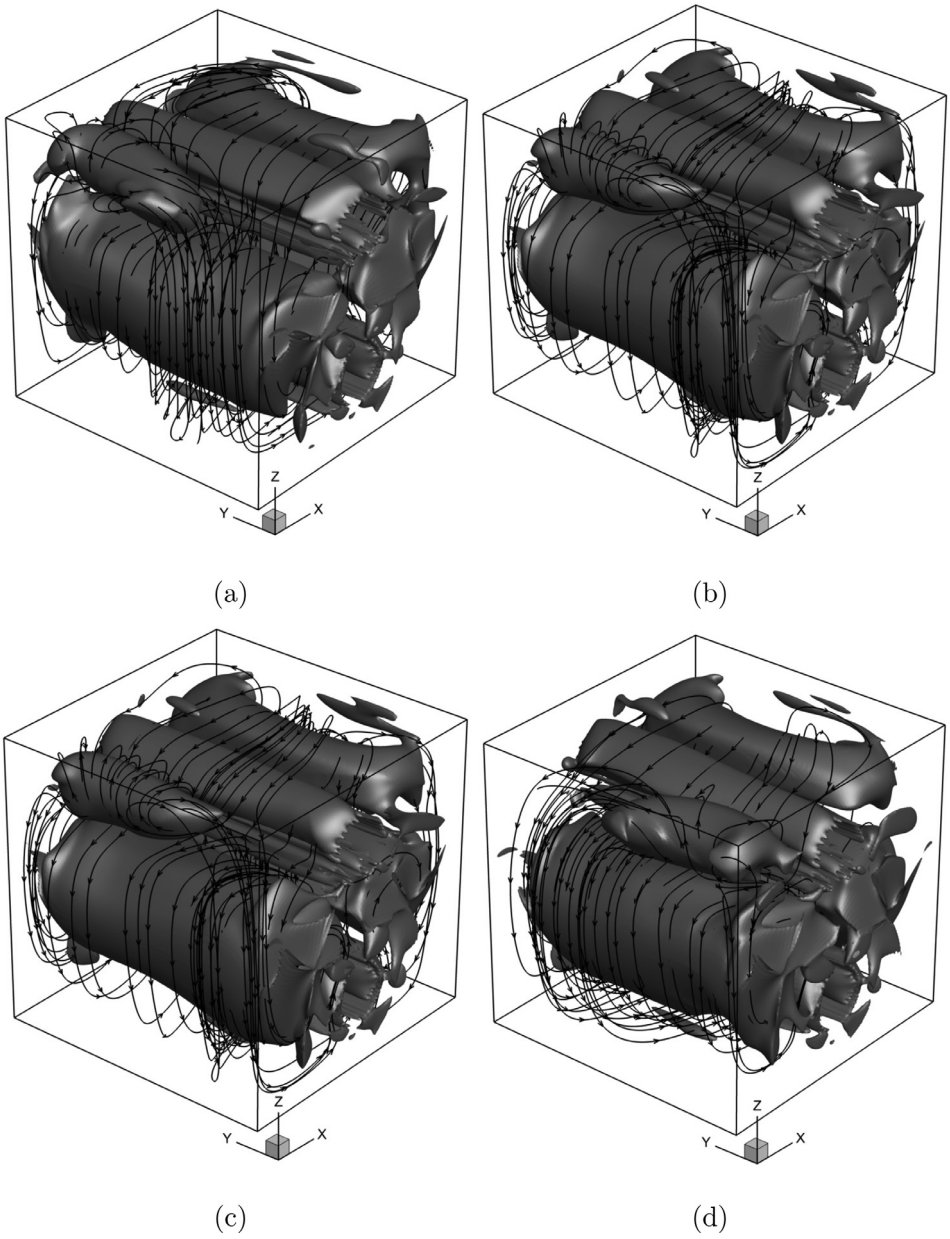

Fig. 10. Snapshots of the spatial distribution of the isosurfaces of $\lambda_2 = -0.1$ superimposed by stream traces shown at four representative instances taken evenly throughout an oscillation period: 1 (a); 2 (b); 3(c); 4(d). The time instances 1–4 are defined in Fig. 9, $\delta = 0.5, Ra = 2 \times 10^5$. The results were obtained on a 200^3 structured uniform grid.

eigenvectors (see e.g. [32,33]). Finally, for every configuration the time histories of the temperature values were monitored at control points symmetrically placed in the vicinity of the midplane $(X-Z)$, as detailed in Table 2.

4.1. Grid independence study

To prove the reliability of the results obtained in the framework of the present research, a grid independence study was conducted. The numerical simulations were performed on 200^3 and 300^3 grids, and the obtained results were compared in terms of the time evolutions of the $\overline{Nu}_h$ and $\overline{Nu}_c$ values averaged over the surfaces of the hot and cold cylinders, respectively, as well as in terms of the time evolution of the temperature values collected at a number of control points whose coordinates are shown in Table 2. Table 3 presents a comparison of the maximal and minimal values of the $\overline{Nu}_h$ and $\overline{Nu}_c$ numbers acquired over a single oscillating period on both grids. The values of the angular frequency corresponding to the oscillating harmonics of the leading mode were also compared. It can be seen that for the entire range of Ra and δ values the maximal deviation between the results does not exceed 1.5%, which verifies the grid independence of the results. In the next step, we compared the evolution characteristics of the pointwise temperatures acquired on the 200^3 and 300^3 grids of different control

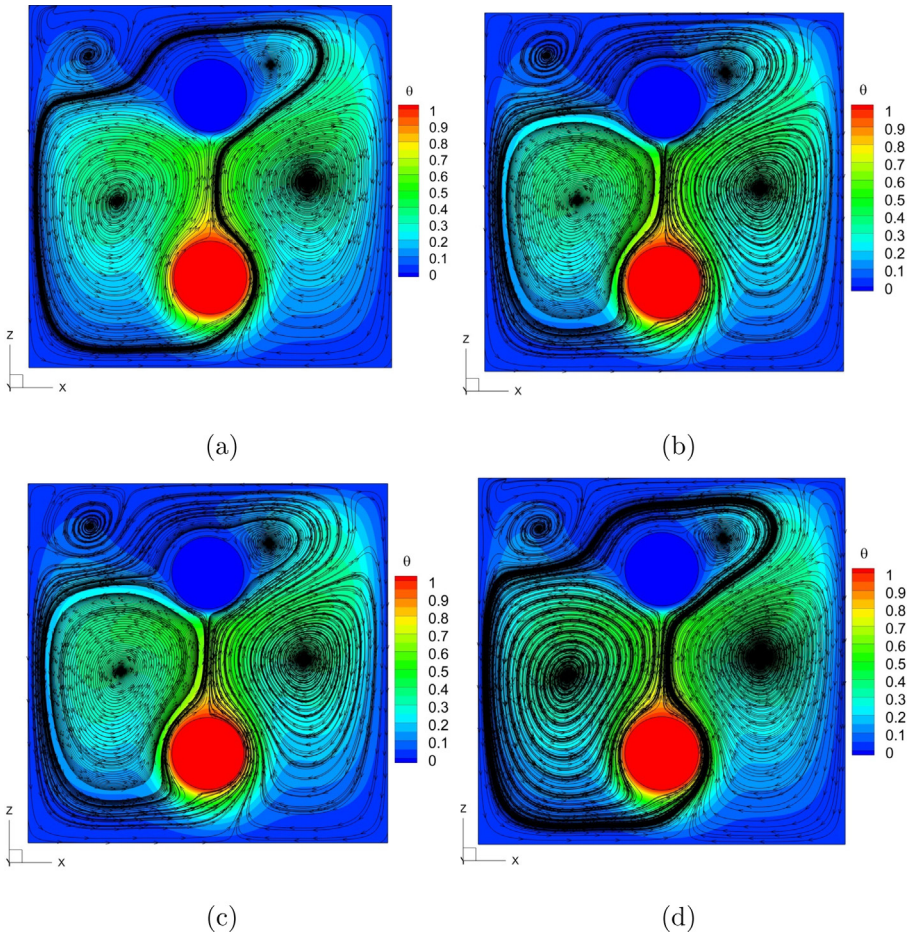

Fig. 11. Snapshots of the spatial temperature distributions at the central cross section $(X-Z)$ shown at four representative instances taken evenly throughout an oscillation period: 1 (a); 2 (b); 3(c); 4(d). The time instances 1–4 are defined in Fig. 9, $\delta = 0.5, Ra = 2 \times 10^5$. The results were obtained on a 200^3 structured uniform grid.

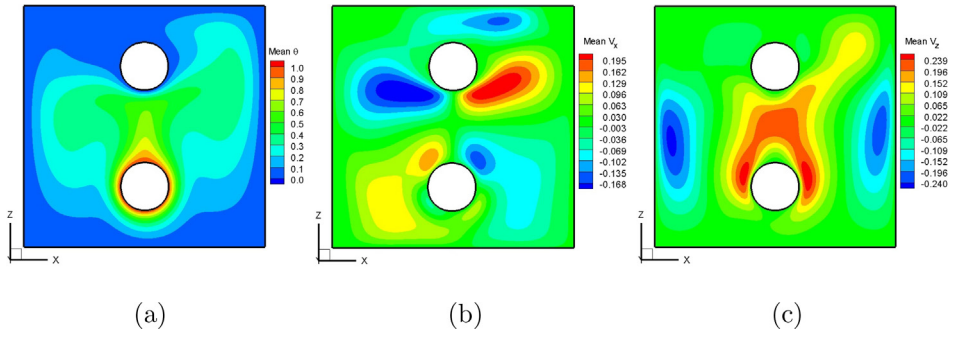

Fig. 12. Distribution of the mean flow characteristics obtained in the mid cross section $(X-Z)$ for: (a) temperature θ; (b) mean v_x velocity component; (c) mean v_z velocity component, $\delta = 0.5, Ra = 2 \times 10^5$. The results were obtained on a 200^3 structured uniform grid.

points, as summarized in Table 2. All the results related to grid verification study are summarized in Table 4. It can be seen that the deviation between the acquired pointwise values does not exceed 1.5% for the entire range of Ra and δ values, which again proves the grid independence of the obtained results.

4.2. Configuration characterized by the value of $\delta = 0.4$

We start our discussion by presenting the time evolution of the $\overline{Nu}_h$ and $\overline{Nu}_c$ numbers averaged over the surfaces of the hot and cold cylinders, respectively, as shown in Fig. 3a and c. The amplitude spectra corresponding to the $\overline{Nu}_h$ and $\overline{Nu}_c$ time evolutions are presented in Fig. 3b and d, respectively. Both time evolutions oscillate with the same value of the angular frequency, $\omega = 0.348$, corresponding to the frequency of the leading eigenmode. Note, also, the presence of the multipliers of the main harmonic whose amplitude is lower by at least an order of magnitude than that of the main harmonic, which is clear evidence of the presence of non-linear effects in the slightly perturbed flow regime. The time evolutions of both $\overline{Nu}_h$ and $\overline{Nu}_c$ are characterized by close values of the amplitudes. The close values were obtained despite the considerable difference (about an order of magnitude) in the average absolute values of $\overline{Nu}_h$ and $\overline{Nu}_c$, which is a direct consequence of holding the four cavity walls at a constant cold temperature T_c. A remarkable result is that the time evolutions of $\overline{Nu}_h$ and $\overline{Nu}_c$ are biased by half a period adjusted for a small phase shift, which can apparently be explained by the flow inertia effects. A deeper insight into the characteristics of the observed instability can be gained by examining the instantaneous distribution of the isosurfaces of $\lambda_2 = -0.1$ (see Fig. 4) characterizing the

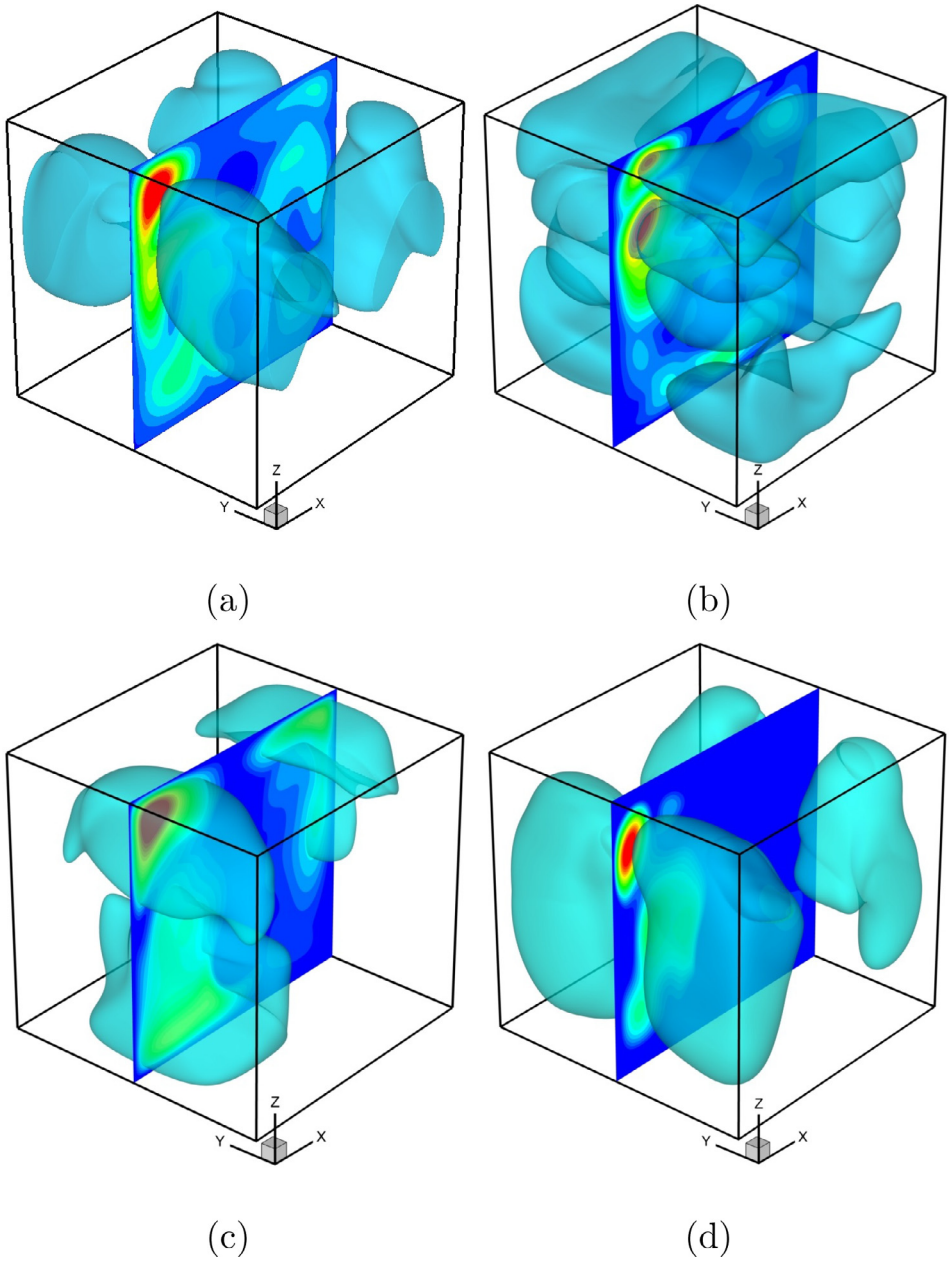

Fig. 13. Isosurfaces of the oscillation amplitudes obtained for: (a) temperature, θ; (b) u_x velocity component; (c) u_y velocity component; and (d) u_z velocity component. The isosurfaces confine the regions characterized by at least 25% of the absolute maximum value. Colors correspond to the relative intensities of the oscillations, $\delta = 0.5, Ra = 2 \times 10^5$. The results were obtained on a 200^3 structured uniform grid.

vortical structures of the flow. Remarkably, at all the time instances, the vortical structures preserve their symmetry with respect to the $(X-Z)$ midplane, while no symmetry is preserved with respect to the $(Y-Z)$ midplane. The symmetry breaking phenomenon is also clearly observed when examining the instantaneous temperature distributions in the midplane $(X-Z)$ of the cubic confinement (see Fig. 5). All the temperature distributions are superimposed with instantaneous particle tracers with the aim of describing the vortical structure of the flow inside the cubic enclosure. It is clearly evident that in the supercritical regime the flow loses its symmetry with respect to the central cross section $(Y-Z)$ throughout the whole oscillation period. Over the oscillation period, the cubical enclosure hosts four vortical structures whose shape and orientation vary with time. At the first time instance (see Fig. 5a), corresponding to the maximum $\overline{Nu}_h$ value, the flow is characterized by two major oppositely rotating vortices located on each side of the central cross section $(Y-Z)$. An additional, and much smaller, counter clockwise vortex is located above and to the right of the surface of the cold cylinder and is driven by a bifurcated hot plume rising from the hot cylinder. The two streams of the hot plume fork close to the bottom of the cold cylinder, reunite to the left of the cold cylinder, and then immediately bifurcate again, each proceeding to the opposite vertical edge of the cube. As the heat flux generated by the hot cylinder decreases, the fourth clockwise-rotating vortex is formed along the horizontal top left edge of the cube, occupying almost the whole cube width (see Fig. 5b). The vortex absorbs the two branches of the bifurcated rising hot plume swirling around the cold cylinder in the central region of the cavity, and redistributes them in a spanwise direction towards the cavity's left and right vertical boundaries. A further decrease in the heat flux generated by the hot cylinder results in considerable weakening of the fourth vortex (see Fig. 5c). As a

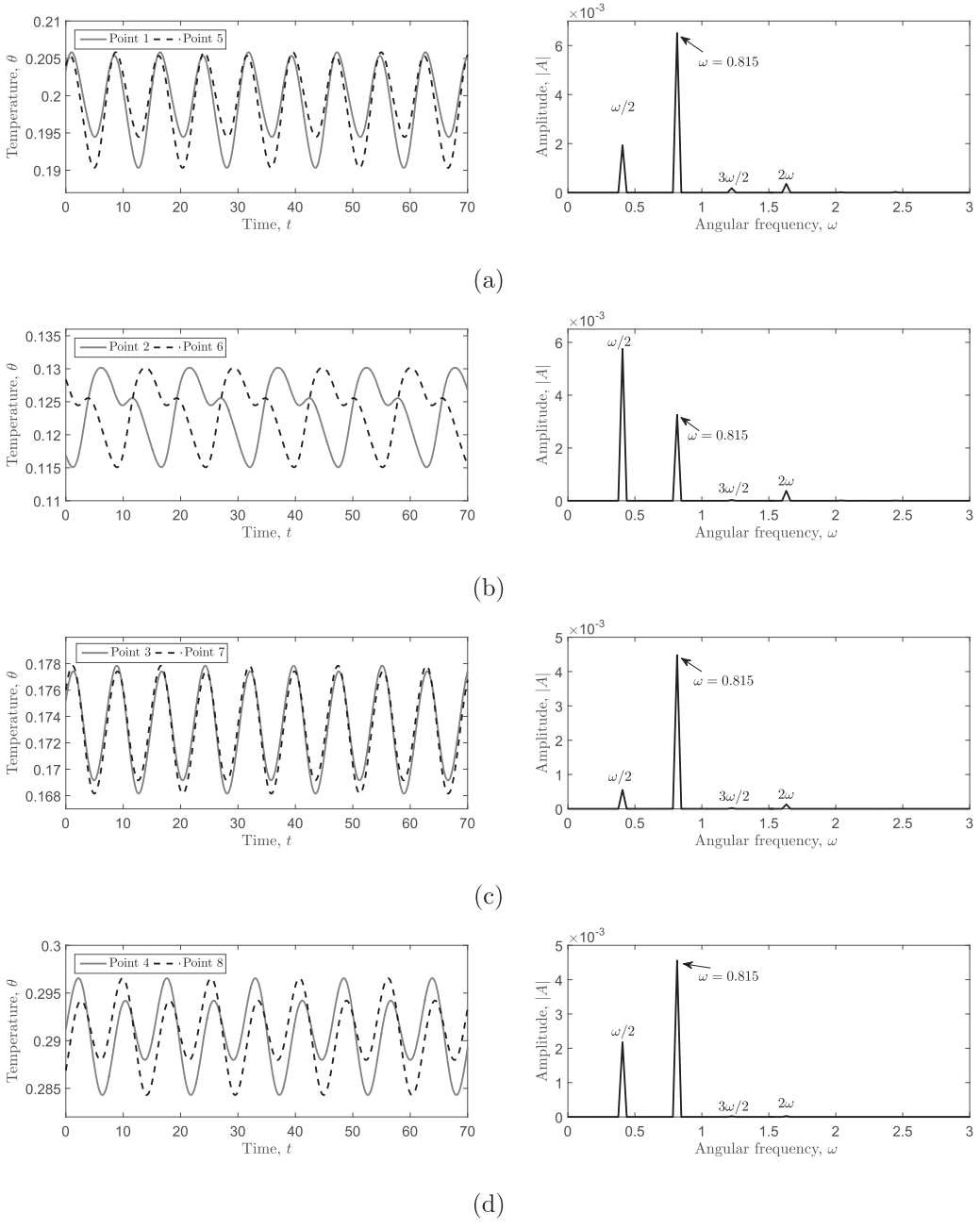

Fig. 14. Temperature monitored at eight points symmetrically distanced relative to the $(X-Z)$ midplane for $\delta = 0.5, Ra = 2 \times 10^5$: (a) time evolution; and (b) Fourier spectrum. The results were obtained on a 200^3 structured uniform grid.

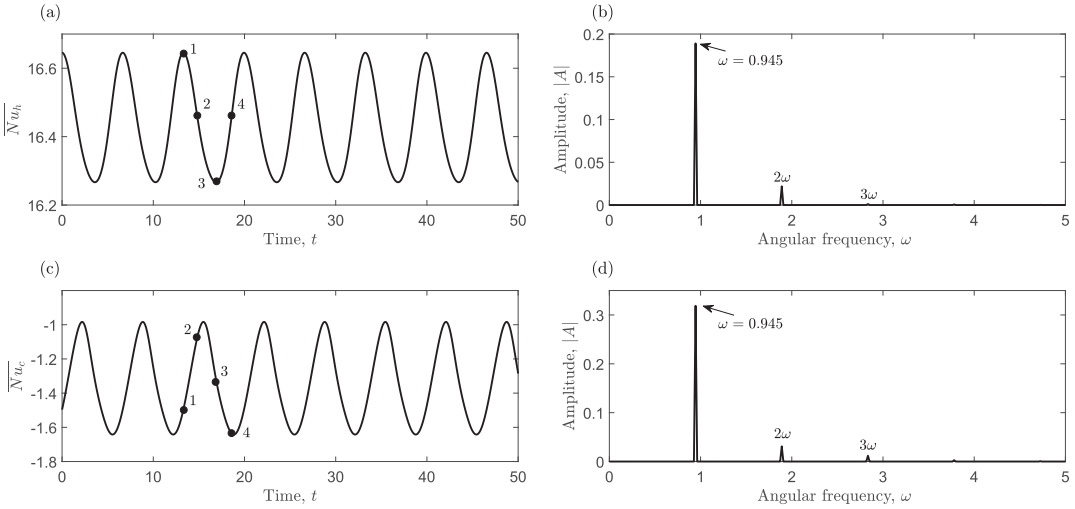

Fig. 15. Time evolution of the averaged $\overline{Nu}_h$ and $\overline{Nu}_c$ numbers and the corresponding Fourier spectra obtained for the values of $\delta = 0.6, Ra = 3.4 \times 10^5$. The results were obtained on a 200^3 structured uniform grid.

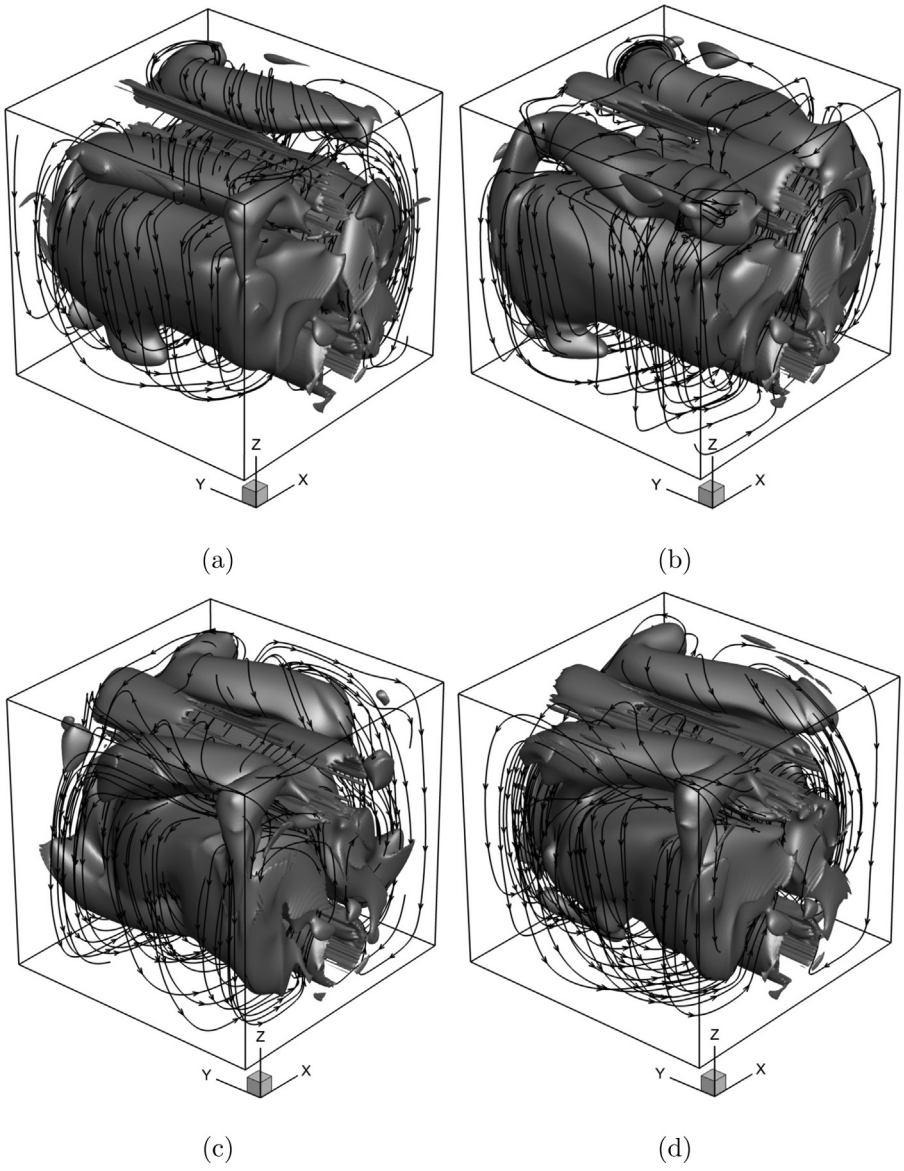

Fig. 16. Snapshots of the spatial distribution of the isosurfaces of $\lambda_2 = -0.1$ superimposed by stream traces shown for four representative instances taken evenly throughout an oscillation period: 1 (a); 2 (b); 3(c); 4(d). Time instances 1–4 are defined in Fig. 15, $\delta = 0.6, Ra = 3.4 \times 10^5$. The results were obtained on a 200^3 structured uniform grid.

result, the convective heat transfer from the hot cylinder to both upper corners of the cubic enclosure reaches its minimum, as evidenced by an intermittent iso-temperature contour in the top left quarter of the midplane $(X-Z)$ of the cubic enclosure. After reaching its minimum at point P. 3 (see Fig. 3a), the heat flux generated by the hot cylinder starts to increase, eventually causing the fourth vortex to vanish (see Fig. 5d), thereby leading to a uniform redistribution of the hot plume flow in a spanwise direction in the vicinity of the cube's top boundary.

To better understand the origin of the observed symmetry breaking phenomenon, the mean flow distribution of all the flow characteristics at the midplane $(X-Z)$ obtained by time averaging of the corresponding flow characteristics over a number of oscillating periods is presented (see Fig. 6). Note that the mean v_y velocity gets close to zero values over the entire midplane and thus is not shown in the figure.

It is now clear that the origin of the previously observed symmetry breaking phenomenon of the instantaneous flow lies in the symmetry breaking of the mean flow distribution of all the flow fields, except for the spanwise v_y component whose value is equal to zero in $(X-Z)$ midplane. As a result, the flow oscillates symmetrically in both parts of the cavity with respect to the $(X-Z)$ midplane, when there is no mixing between the liquids in the two parts of the cavity. To provide an idea of the spatial distribution of perturbation corresponding to the leading eigenvector of the perturbed flow, the spatial distribution of the flow oscillation amplitudes for the temperature and all three velocity components calculated at $Ra = 2 \times 10^5$ are presented below (see Fig. 7).

The contours of the oscillating amplitudes of the slightly supercritical flow resemble the spatial distribution of the leading eigenvector of the corresponding flow field (see e.g.[24,33]). The presented data is obtained by subtracting the mean flow values from the corresponding maximum values of every flow field attained at each grid point over a single oscillation period. Isosurfaces confining the regions in which the values of the oscillation amplitudes reach at least 25% of the absolute maximum are shown in Fig. 7 for each flow field. It is evident that the oscillating amplitudes, calculated for the temperature θ and the velocity components u_x and u_z fields attain their maximum values on the $(X-Z)$ midplane. In contrast, the u_y velocity component is characterized by zero values of the oscillating amplitudes on the $(X-Z)$ midplane. It is remarkable that, despite the symmetry break relative to the $(Y-Z)$ midplane, both the spatial distributions of the λ_2 criterion (see Fig. 5) and of the oscillating amplitudes for all the flow fields retain their symmetry relative to the $(X-Z)$ midplane. As a result, it can be expected that the characteristics (both qualitative and quantitative) of the instability observed for the 3D configuration will also be reproduced by the corresponding 2D analysis.

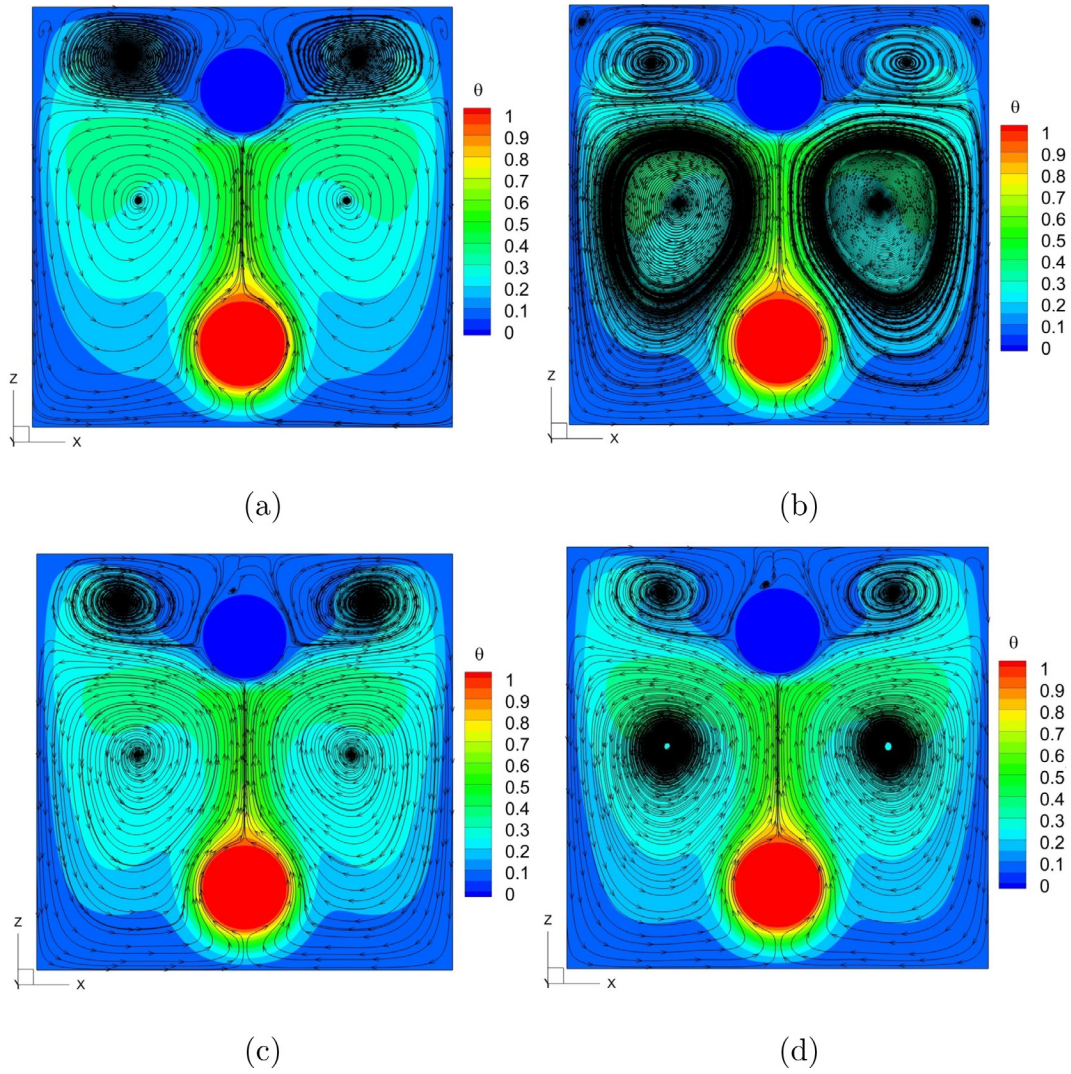

Fig. 17. Snapshots of the spatial temperature distributions at the central cross section $(X-Z)$ shown for four representative instances taken evenly throughout an oscillation period: 1 (a); 2 (b); 3(c); 4(d). Time instances 1–4 are defined in Fig. 15, $\delta = 0.6, Ra = 3.4 \times 10^5$. The results were obtained on a 200^3 structured uniform grid.

To further verify that the observed global reflectional symmetry is preserved over the whole oscillation period, we monitor the temperature signals at eight points (see Table 2 for locataion of each point) symmetrically distanced relative to the $(X-Z)$ midplane (see Fig. 8).

It can clearly be seen that all the time signals completely coincide at each time step throughout the whole oscillation period. It is also remarkable that for each signal, the frequency of the main oscillating harmonic is the same as that corresponding to the averaged $\overline{Nu}_h$ and $\overline{Nu}_c$ values, which verifies the fact that for the above configuration both Nusselt numbers can safely be used as control parameters for monitoring steady-unsteady transition. Based on all the above, it can be concluded that the observed oscillatory instability exhibits symmetry breaking of the mean flow with respect to the $(Y-Z)$ midplane, while the global reflectional symmetry of the oscillatory flow is preserved with respect to the $(X-Z)$ midplane.

4.3. Configuration characterized by the value of $\delta = 0.5$

We now perform a similar analysis to characterize the instability observed for $\delta = 0.5$ and $Ra = 2 \times 10^5$. The time evolution of the $\overline{Nu}_h$ and $\overline{Nu}_c$ numbers averaged over the surfaces of the hot and cold cylinders, with the corresponding frequency spectra, are presented in Fig. 9. Note that similarly to the previous configuration, the signals monitored for both $\overline{Nu}$ values are governed by a single oscillating harmonic and its multipliers. At the same time, the value of the harmonic $\omega = 0.815$ is more than twice that observed for the previous configuration, giving rise to an expectation of a qualitatively different character of the observed instability.

In fact, a closer look at the instantaneous distribution of the isosurfaces of $\lambda_2 = -0.1$ shown in Fig. 10 reveals that in contrast to the configuration characterized by $\delta = 0.4$ at none of time instances shown in Fig. 10 does the vortex occupying the left top corner of the cavity symmetrically extend from both sides of the midplane $(X-Z)$. On the contrary, at each time instance, it mostly occupies the space on only one side of the cross section. The qualitatively different character of the observed instability is further confirmed by examining the corresponding temperature distribution in the midplane $(X-Z)$ of the cubic confinement with superimposed stream tracers, as shown in Fig. 11. As expected, the midplane $(X-Z)$ of the configuration under discussion here hosts an additional (fourth) clockwise-rotating vortex at the top left quarter of the cross section throughout the whole oscillating cycle; this vortex comprises an instantaneous footprint of the oscillating vortical structure shown in Fig. 10. It is also remarkable that the time variation of the temperature contours in this cross section

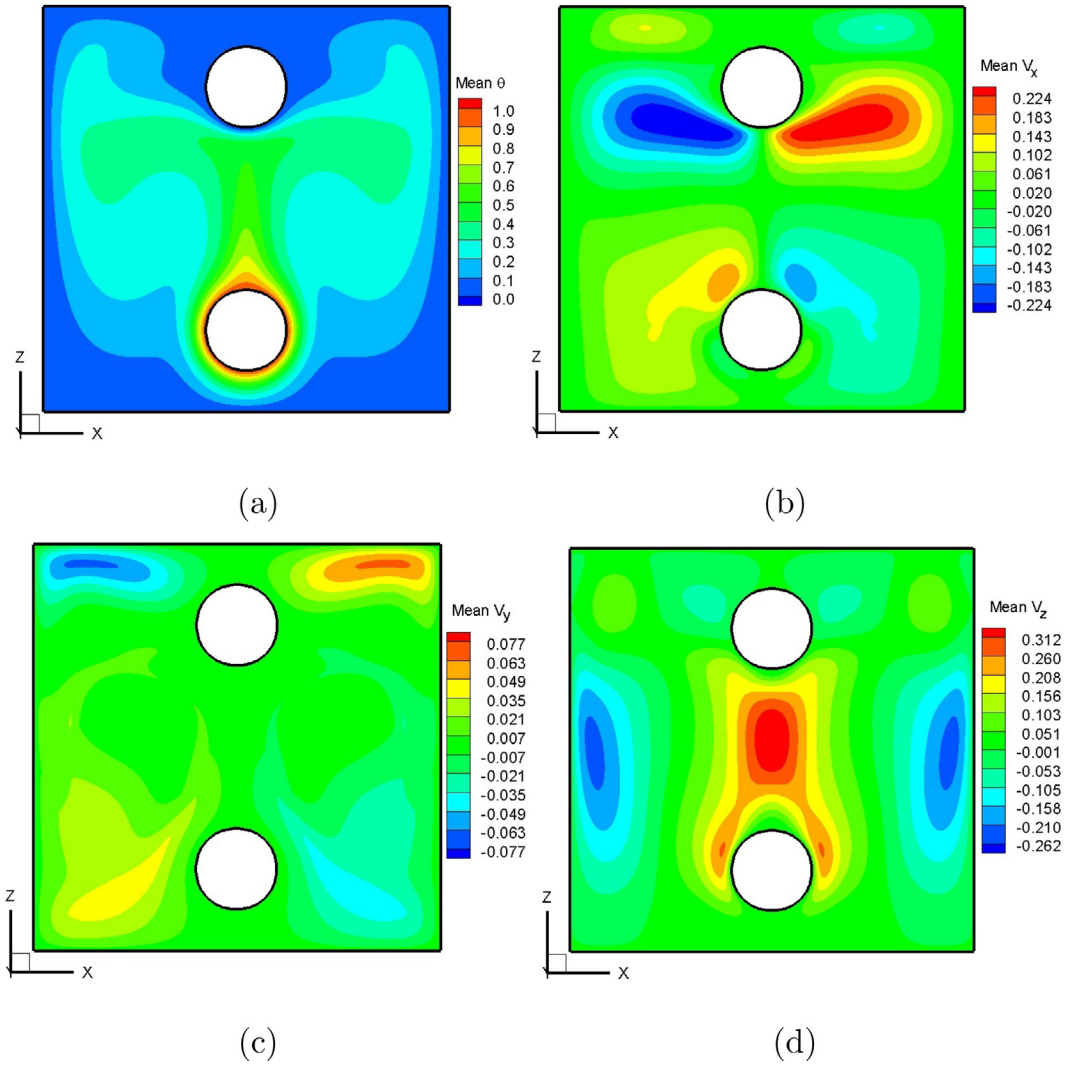

Fig. 18. Distribution of the mean flow characteristics obtained in the mid cross section $(X-Z)$ for: (a) temperature θ; (b) mean v_x velocity component; (c) mean v_y velocity component; (d) mean v_z velocity component, $\delta = 0.6, Ra = 3.4 \times 10^5$. The results were obtained on a 200^3 structured uniform grid.

is almost indistinguishable. It is important to note that the phenomenon is characterized by fully 3D dynamics and therefore cannot be reproduced (even qualitatively) by the corresponding 2D analysis.

The mean flow distribution of all the flow fields, shown in Fig. 12, resembles the corresponding flow distribution obtained for the previous flow configuration characterized by $\delta = 0.4$ (i.e., qualitatively the same symmetry-breaking phenomenon with respect to the $(Y-Z)$ midplane of mean temperature θ and v_x and v_y velocity components, while the mean values of the v_y component are close to zero and are thus not shown). Similarly to the previous configuration, no mixing of the fluid located on both sides of the cavity midplane $(X-Z)$ takes place. At the same time, further investigation of the isosurfaces of the oscillation amplitudes and of the temporal-spectral characteristics of the temperatures monitored at eight control points (see Figs. 13 and 14, respectively) reveals an entirely different mechanism of the instability onset that characterises the present configuration.

As a result of increasing the value of δ from $\delta = 0.4$ to $\delta = 0.5$, the impact of the boundary of the cold cylinder in suppressing the momentum of the plume rising from the hot cylinder decreases. Consequently, the momentum of the hot plume developing and reaching the top boundary of the cube is higher for the $\delta = 0.5$ configuration than for its $\delta = 0.4$ counterpart: the higher momentum of the flow can no longer be dissipated by the cavity walls in a manner that would provide the reflectional symmetry oscillations observed for $\delta = 0.4$. As a result, the flow undergoes bifurcation characterized by spatio-temporal symmetry H half a period apart, preserving the Y_2 symmetry group [41] and formally reading:

$$H\boldsymbol{u}(\boldsymbol{X}', t) = K_{\boldsymbol{Y}'}(\boldsymbol{X}, t + T/2) = (u_{X'}, -u_{Y'}, u_{Z'})(X', -Y', Z', t + T/2), \quad (11)$$

with H-symmetric base flow $H\bar{\boldsymbol{u}}(\boldsymbol{X}') = K_{Y'}\bar{\boldsymbol{u}}(\boldsymbol{X}')$, where $K_{Y'}$ is the spatial reflection: $Y' \to -Y', u_{Y'} \to -u_{Y'}$ and T is the period of the per-

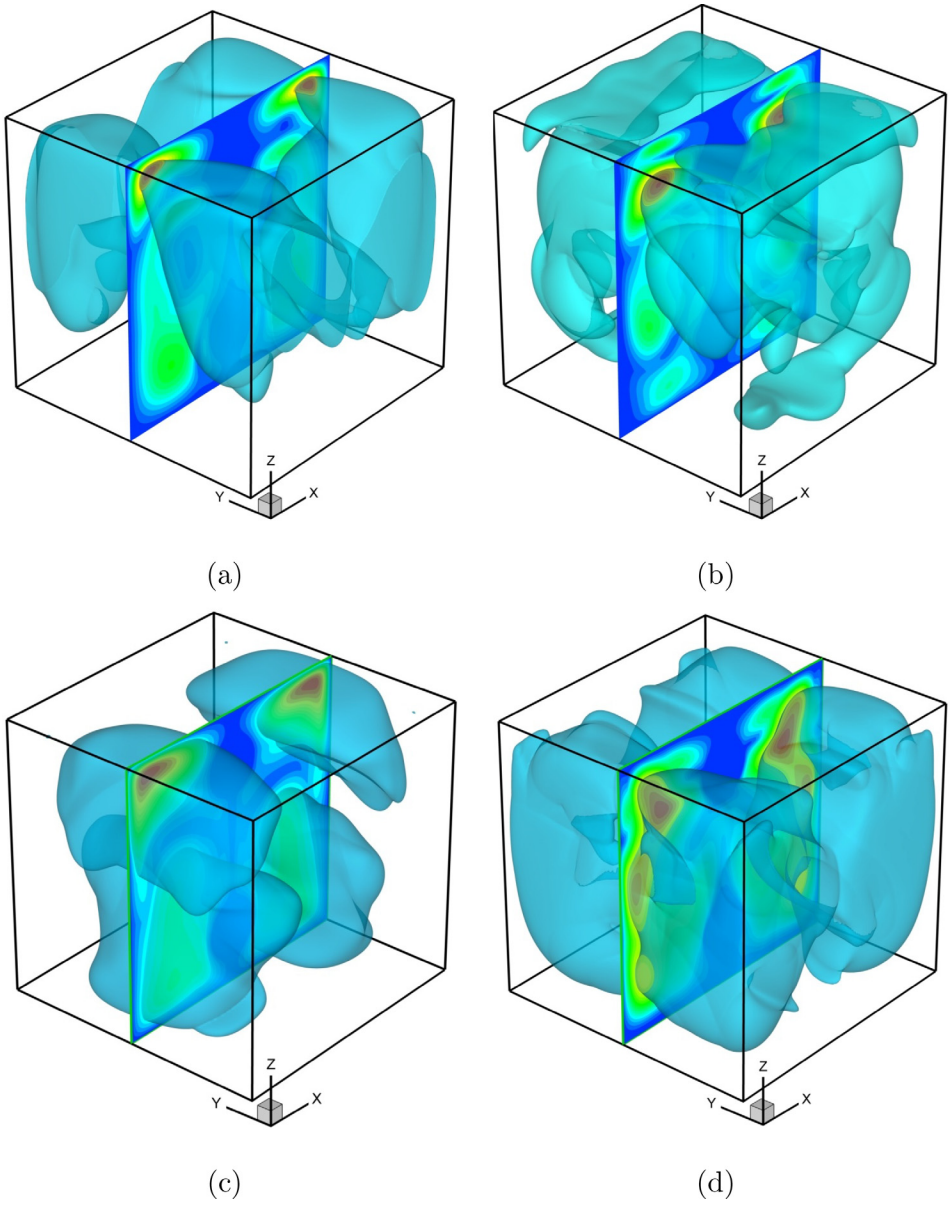

Fig. 19. Isosurfaces of the oscillation amplitudes obtained for: (a) temperature, θ; (b) u_x velocity component; (c) u_y velocity component; and (d) u_z velocity component. The isosurfaces confine the regions characterized by at least 25% of the absolute maximum value. Colors correspond to the relative intensities of the oscillations, $\delta = 0.6, Ra = 3.4 \times 10^5$. The results were obtained on a 200^3 structured uniform grid.

turbed flow oscillations. Note that exactly the same scenario was revealed with respect to the bifurcated shear flow inside a diagonally lid driven cavity [33].

The proposed scenario for the observed instability is confirmed by the symmetry of the oscillation amplitudes, as demonstrated in Fig. 13 and by examination of the time evolution history of the temperature signals monitored at all symmetrically located points, as shown in Fig. 14.

It can be clearly seen that the time evolutions monitored at all the point pairs are half a period apart, up to a small offset apparently caused by the non-negligible inertial effects of the flow. The most important observation is that pertaining to the non-negligible and even dominant value of the half harmonic amplitude clearly seen in Fig. 15(a) and (d) and in Fig. 15(b), respectively. The presence of the half harmonic could have been attributed to the secondary Hopf bifurcation setting in via period doubling, in accordance with the Feigenbaum scenario. However, we argue that the observed bifurcated flow corresponds to the first, rather than to the second Hopf bifurcation and that the harmonic value $\omega = 0.4075$ is the value of the oscillating angular frequency of the leading unstable eigenmode. In fact, half harmonics dominate in signals acquired at control points P.2 and P.6 located inside the core of the fourth clock-wise rotating vortex undergoing symmetrical oscillations from both sides relative to the symmetry $(X - Z)$ midplane, while the non-negligible footprint of the half harmonics is also recognized for signals monitored in other pairs of control points. It is also noteworthy that both $\overline{Nu}_h$ and $\overline{Nu}_c$ numbers oscillate with a doubled value of the frequency as they reflect the symmetrical oscillation of the fourth vortex switching its position relative to the symmetry $(X - Z)$ cross section with a doubled frequency.

To summarize, the value of the critical oscillating harmonic for the present configuration is characterized by the value of $\omega = 0.4075$ rather than by $\omega = 0.815$. This value is not so different from the value of $\omega = 0.348$ characterizing the oscillatory instability the previous configuration characterized by $\delta = 0.4$, although

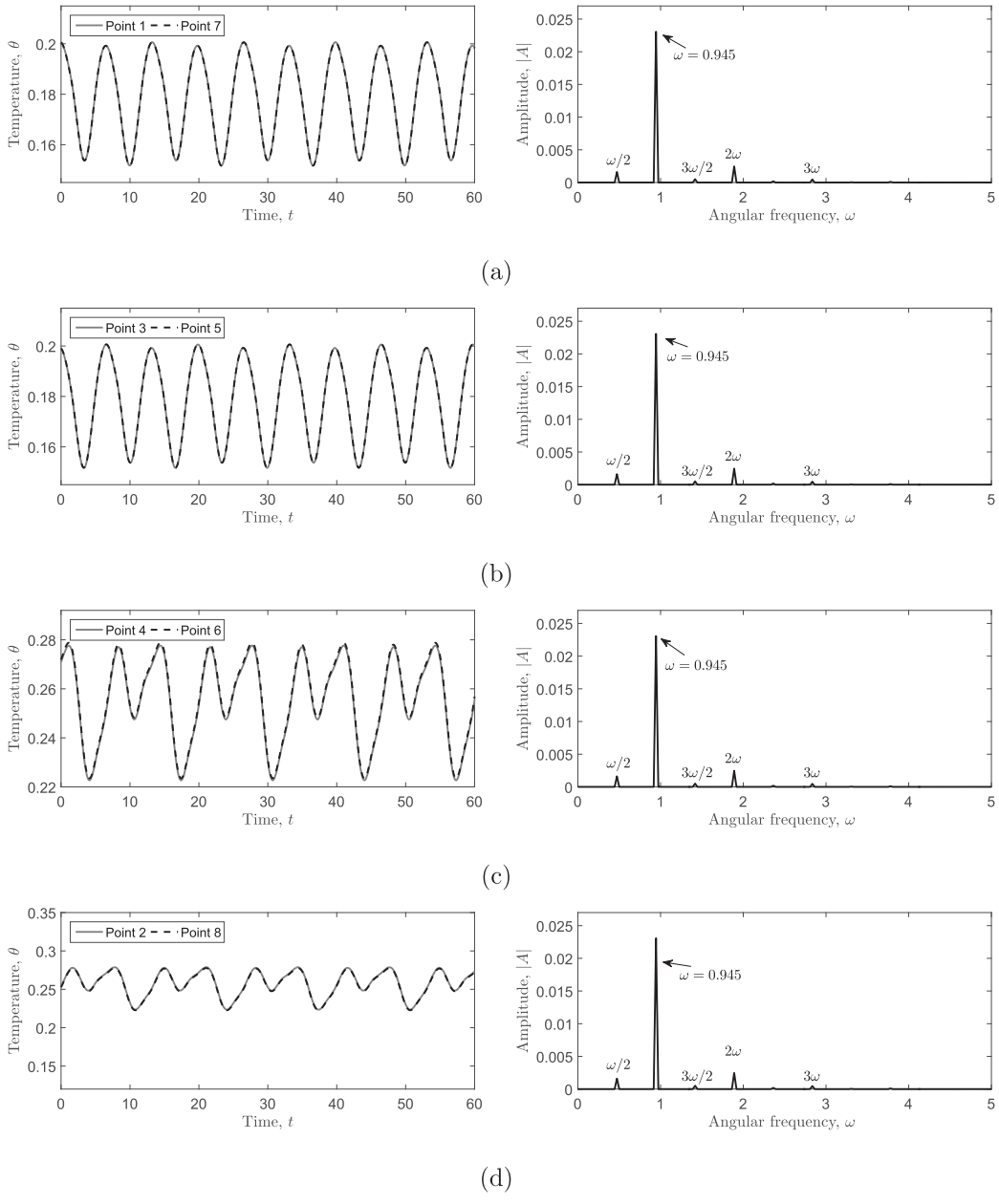

Fig. 20. Temperature monitored at eight points symmetrically distanced relative to the $(X - Z)$ midplane for $\delta = 0.6, Ra = 3.4 \times 10^5$: (a) time evolution; and (b) Fourier spectrum. The results were obtained on a 200^3 structured uniform grid.

the onsets of the two instabilities may be attributed to entirely different mechanisms.

4.4. Configuration characterized by the value of $\delta = 0.6$

To further investigate the influence of the vertical distance between the hot and the cold cylinders on the instability mechanism, the configuration characterized by the value of $\delta = 0.6$ is considered. Following the steps performed for the previous configurations, we first analyze the time evolution of the $\overline{Nu}_h$ and $\overline{Nu}_c$ values averaged over the surfaces of the hot and cold cylinders, respectively, as presented in Fig. 15. The time evolution of the two time averaged $\overline{Nu}$ values does not differ significantly from the corresponding signals acquired for the value of $\delta = 0.5$. The time evolution is periodic and is determined by the main harmonic value equal to $\omega = 0.945$. As a result of the non-linearity of the supercritical flow regime, the main harmonic multipliers are clearly distinguishable in the corresponding Fourier spectrum (see Fig. 15b and d). The mean values of the two $\overline{Nu}$ numbers are close to those obtained for the previous ($\delta = 0.5$) configuration, but the amplitudes of the Nu values at $\delta = 0.6$ are significantly (more than twice) higher, apparently indicating the presence of a different instability mechanism.

The above assumption is supported by a further examination of the isosurfaces of the $\lambda_2 = -0.1$ criterion, as shown in Fig. 16, and of the corresponding temperature distribution in the midplane $(X - Z)$ of the cubic confinement superimposed by the particle tracers, as presented in Fig. 17. It can be seen that at each time instance the midplane hosts four major vortices. The two larger vortices are formed by a hot plume rising from the surface of the hot cylinder, and the two smaller vortices are formed by a cold stream descending along the surface of the cold cylinder. The hot and cold vortices interact with one another through the dynamic interfaces whose position and orientation vary over the oscillation period. Contrary to the two previous configurations, it can be clearly seen that both the temperature distribution and the stream traces exhibit global reflection symmetry in the $(X - Z)$ midplane relative to the vertical centerline at each time instance. Also compared to the two previous configurations, the spatial distribution of instantaneous isosurfaces of the $\lambda_2 = -0.1$ criterion and the corresponding stream tracers (see Fig. 16) both exhibit diagonal reflection symmetry with respect to the $(Y - Z)$ midplane and also with respect to two main diagonal planes passing through the vertical opposite edges of the cavity; this finding is worthy of further investigation.

A deeper understanding of the characteristics of the observed instability can be gained by examining the distributions of the mean temperature and of each velocity field in the $(X - Z)$ midplane shown in Fig. 18. Contrary to the configurations characterized by $\delta = 0.4$ and $\delta = 0.5$, the present configuration is characterized, first, by non-zero values of the mean spanwise velocity component v_y, and second, by a symmetric distribution of the temperature and v_z velocity fields and an anti-symmetric distribution of the v_x and v_y velocity fields. The first observation means that the liquid separated by the $(X - Z)$ plane undergoes a mixing phenomenon through this plane, while the second observation allows us to conclude that the bifurcated flow is preceded by a steady state preserving the symmetry (and anti-symmetry) of all the flow characteristics with respect to the $(Y = Z)$ midplane.

As expected, the symmetry with respect to the $(X - Z)$ and $(Y - Z)$ mid planes is also preserved for the spatial distribution of the oscillation amplitudes for all the flow fields (see Fig. 19). The unexpected finding is that the observed reflectional symmetry is actually not dependent on the orientation of Y and X, as it persists in all the planes passing through the line for all the oscillation amplitudes. The same observations were also made for all the instantaneous distributions of the λ_2 criterion (see Fig. 16). Note also that, similarly to the previous configuration, the observed phenomenon is fully 3D and therefore cannot be revealed by the corresponding 2D analysis. To determine whether the observed symmetry persists for each time step or only for some specific time instances, we further investigated the time evolution history of the temperature acquired at eight control points, symmetrically distanced relative to the vertical centerline, as shown in Fig. 20.

It can be seen that the signals acquired for all four pairs of the control points coincide, clearly indicating that the flow exhibits reflectional symmetry relative to the centerline at each time step (see Fig. 20). The flow oscillates with the same angular frequency, $\omega = 0.945$, as the averaged values of the hot $\overline{Nu}_h$ and cold $\overline{Nu}_c$ values. Small peaks of the doubled time period, and its multiplier, can be seen at the $\omega/2$ and $3\omega/2$ values of the corresponding Fourier spectrum, respectively. We speculate that the peaks are the outcome of the secondary Hopf bifurcation, in accordance with the Feigenbaum scenario, which means that the observed bifurcation flow should have been formally studied at a Rayleigh value smaller than $Ra = 3.4 \times 10^5$. At the same time, the absolute values of the amplitudes of the secondary peaks are very small and do not exceed 15% of the corresponding amplitude values obtained for the first Hopf bifurcation. It can thus be safeley stated that the characteristics of the primary instability described in the present section for the values of $\delta = 0.6$ and $Ra = 3.4 \times 10^5$ are not affected, nonetheless the flow has apparently undergone a secondary Hopf bifurcation.

5. Conclusions

Three-dimensional natural convection flow around a tandem of cold and hot vertically aligned cylinders placed inside a cold cubic enclosure was thoroughly investigated as a function of the distance between the cylinders in terms of the values of the major oscillating harmonics, the isosurfaces of the oscillating amplitudes, and the global reflectional symmetries of the mean and supercritical flows. It was found that the distance δ between the cylinders plays an important role in determining the characteristics of the instability mechanisms governing the oscillatory flow. In particular, three different instability mechanisms were revealed and characterized for the values of $\delta = 0.4, 0.5$ and 0.6.

It was found that for the values of $\delta = 0.4$ and $Ra = 2 \times 10^5$ the slightly perturbed flow oscillates with an angular frequency equal to $\omega = 0.348$, and the mean flow loses its reflectional symmetry relative to the $(Y - Z)$ midplane. At the same time, the global reflectional symmetry of the oscillating flow is preserved relative to the $(X - Z)$ midplane at each time instance. The slightly supercritical flow obtained by further increasing the distance between the cold and the hot cylinders to $\delta = 0.5$, while keeping the same value of the Ra number, is governed by a different instability mechanism, which is characterized by a higher value of the main oscillating harmonic, equal to $\omega = 0.4075$. In addition, for this configuration the flow is characterized by the global reflectional symmetry of the mean flow and by an offset of half a period of the flow characteristics relative to the symmetry midplane $(X - Z)$. The mean flow of all the flow characteristics except for the mean flow of the v_y velocity component loses its symmetry in the $(X - Z)$ midplane, while the mean v_y velocity component is equal to zero in the $(X - Z)$ midplane. Therefore, there is no mixing of the fluid with respect to the $(X - Z)$ midplane for both the $\delta = 0.4$ and $\delta = 0.5$ configurations. Finally, the third configuration, whose slightly perturbed flow was obtained for the value of $\delta = 0.6$

at $Ra = 3.4 \times 10^5$, is characterized by a value of the angular frequency of the main harmonic equal to $\omega = 0.945$. Both mean and perturbed flows exhibit global reflectional symmetry relative to the vertical centerline, which is preserved with respect to all the planes passing through the line. It is also noteworthy that in all the configurations studied in the framework of the current study the $\overline{Nu}_h$ values (both instantaneous and averaged over the time of oscillating period) are higher by an order of magnitude than the corresponding $\overline{Nu}_c$ values, which is a direct consequence of mainting the conducting walls of the cubic cavity at the cold temperature T_c.

The current study clearly demonstrates a rich variety of instability scenarios typical of the configuration under consideration; these scenarios include the reflectional symmetry of the bifurcated flow for $\delta = 0.4$, the $K_{Y'}$ symmetry with a half a period apart of the bifurcated flow for $\delta = 0.5$, and the reflectional symmetry of the bifurcated flow preserved with respect to all the planes passing through the vertical center line for $\delta = 0.6$. The results obtained could be useful for verification of future numerical studies focusing on building detailed stability diagrams based on the technique of linear stability analysis.

Declaration of Competing Interest

The authors declared that there is no conflict of interest.

Acknowledgement

The study was funded by GIF – German Israel Foundation, under contract number: I-2471–405.10/2017.

References

[1] I. Ishihara, R. Fukui, R. Matsumoto, Natural convection in a vertical rectangular enclosure with symmetrically localized heating and cooling zones, Int. J. Heat Fluid Flow 23 (2002) 366–372.
[2] A. da Silva, S. Lorente, A. Bejan, Optimal distribution of discrete heat sources on a wall with natural convection, Int. J. Heat Mass Transf. 47 (2004) 203–214.
[3] S. Banerjee, S. Mukhopadhyay, A. Ren, R. Ganguly, Natural convection in a biheater configuration of passive electronic cooling, Num. Heat Transf. A 47 (2008) 1516–1527.
[4] Q. Deng, Fluid flow and heat transfer characteristics of natural convection in square cavities due to discrete source–sink pairs, Int. J. Heat Mass Transf. 51 (2008) 5949–5957.
[5] F. Selimefendigil, H. Öztop, Natural convection and entropy generation of nanofluid filled cavity having different shaped obstacles under the influence of magnetic field and internal heat generation, J. Taiwan Inst. Chemic. Engin. 56 (2015) 42–56.
[6] L. Kolsi, H. Öztop, A. Alghamdi, N. Abu-Hamdeh, N. Borjini, H. Aissia, A computational work on a three dimensional analysis of natural convection and entropy generation in nanofluid filled enclosures with triangular solid insert at the corners, J. Molec. Liquids. 218 (2016) 260–274.
[7] M. Ismael, T. Armaghani, A. Chamkha, Conjugate heat transfer and entropy generation in a cavity filled with anano fluid-saturated porous media and heated by a triangular solid, J. Taiwan Inst. Chemic. Engin. 59 (2016) 138–151.
[8] F. Garoosi, F. Hoseininejad, M.M. Rashidi, Numerical study of natural convection heat transfer in a heat exchanger filled with nanofluids, Energy 109 (2016) 664–678.
[9] T. Höhne, S. Kliem, U. Bieder, Modeling of a buoyancy-driven flow experiment at the ROCOM test facility using the CFD codes CFX-5 and Trio_U, Nucl. Eng. Des. 236 (2006) 1309–1325.
[10] U. Bieder, F. Falk, G. Fauchet, CFD analysis of the flow in the near wake of a generic PWR mixing grid, Ann. Nucl. Energy 82 (2015) 169–178.
[11] A. Renfer, M.K. Tiwari, R. Tiwari, F. Alfieri, T. Brunschwiler, B. Michel, D. Poulikakos, Microvortex-enhanced heat transfer in 3D-integrated liquid cooling of electronic chip stacks, Int. J. Heat Mass Transfer 65 (2013) 33–43.
[12] F. Alfieri, M.K. Tiwari, A. Renfer, T. Brunschwiler, B. Michel, D. Poulikakos, Computational modeling of vortex shedding in water cooling of 3D integrated electronics, Int. J. Heat Fluid Flow 44 (2013) 745–755.
[13] A. Baïri, E. Zarco-Pernia, J.-M.G. De María, A review on natural convection in enclosures for engineering applications. the particular case of the parallelogrammic diode cavity, Appl. Therm. Eng. 63 (2014) 304–322.
[14] R. Huang, H. Wu, An immersed boundary-thermal lattice Boltzmann method for solid–liquid phase change, J. Comput. Phys. 277 (2014) 305–319.
[15] Y. Huo, Z. Rao, Investigation of solid-liquid phase change in the spherical capsule using axisymmetric lattice Boltzmann model, Int. J. Heat Mass Transfer 119 (2018) 1–9.
[16] S.H. Hussain, A.K. Hussein, Numerical investigation of natural convection phenomena in a uniformly heated circular cylinder immersed in square enclosure filled with air at different vertical locations, Int. Commun. Heat Mass Transfer 37 (2010) 1115–1126.
[17] H. Lee, J. Doo, M. Ha, H. Yoon, Effects of thermal boundary conditions on natural convection in a square enclosure with an inner circular cylinder locally heated from the bottom wall, Int. J. Heat Mass Transf. 65 (2013) 435–450.
[18] Y. Park, M. Ha, C. Choi, J. Park, Natural convection in a square enclosure with two inner circular cylinders positioned at different vertical locations, Int. J. Heat Mass Transf. 77 (2014) 501–518.
[19] Y. Park, M. Ha, J. Park, Natural convection in a square enclosure with four circular cylinders positioned at different rectangular locations, Int. J. Heat Mass Transf. 81 (2015) 490–511.
[20] Y.M. Seo, Y.G. Park, M. Kim, H.S. Yoon, M.Y. Ha, Two-dimensional flow instability induced by natural convection in a square enclosure with four inner cylinders. part i: Effect of horizontal position of inner cylinders, Int. J. Heat Mass Transf. 113 (2017) 1306–1318.
[21] Y.M. Seo, G.S. Mun, Y.G. Park, M.Y. Ha, Two-dimensional flow instability induced by natural convection in a square enclosure with four inner cylinders. part ii: Effect of various positions of inner cylinders, Int. J. Heat Mass Transf. 113 (2017) 1319–1331.
[22] S. Hadi, M. Rahomey, Comparison of natural convection around a circular cylinder with different geometries of cylinders inside a square enclosure filled with cu-nanofluid superposed porous-nanofluid layers, J. Heat Transfer (2018).
[23] Y. Feldman, Oscillatory instability of 2D natural convection flow in a square enclosure with a tandem of vertically aligned cylinders, Fluid Dyn. Res. 50 (2018) 051410.
[24] Y. Gulberg, Y. Feldman, Flow control through use of heterogeneous porous media: Smart passive thermo-insulating materials, Int. J. Therm. Scien. 110 (2016) 369–382.
[25] S. Idan, Y. Feldman, "Smart" passive thermal insulation of confined natural convection heat transfer: An application to hollow construction blocks, Appl. Therm. Eng. 124 (2017) 1328–1342.
[26] Y.M. Seo, J.H. Doo, M.Y. Ha, Three-dimensional flow instability of natural convection induced by variation in radius of inner circular cylinder inside cubic enclosure, Int. J. Heat Mass Transf. 95 (2016) 566–578.
[27] Y.M. Seo, J.M. Lee, Y.G. Park, M.Y. Ha, Effect of horizontal spacing between inner circular cylinders on three-dimensional natural convection in rectangular channel, Heat Mass Transf. 54 (2018) 537–551.
[28] J. Lee, On the three-dimensional effect for natural convection in horizontal enclosure with an adiabatic body: Review from the 2D results and visualization of 3D flow structure, Int. Com. Heat Mass Transfer 92 (2018) 31–38.
[29] J. Lee, Numerical simulation of natural convection in a horizontal enclosure: Part I. On the effect of adiabatic obstacle in middle, Int. J. Heat Mass Transfer 124 (2018) 220–232.
[30] H. Dijkstra, F. Wubs, A. Cliffe, E. Doedel, I. Dragomirescu, B. Eckhardt, A. Gelfgat, A. Hazel, V. Lucarini, A. Salinger, E.T. Phipps, J. Sanchez-Umbria, H. Shuttelaars, L. Tuckerman, U. Thile, Numerical bifurcation methods and their application to fluid dynamics: analysis beyound simulation, Commun. Comput. Phys. 15 (2014) 1–45.
[31] Y. Feldman, Semi-implicit direct forcing immersed boundary method for incompressible viscous thermal flow problems: a Schur complement approach, Int. J. Heat Mass Transf. 127 (2018) 1267–1283.
[32] Y. Feldman, A.Y. Gelfgat, Oscillatory instability of a three-dimensional lid-driven flow in a cube, Phys. Fluids 22 (2010) 093602.
[33] Y. Feldman, Theoretical analysis of three-dimensional bifurcated flow inside a diagonally lid-driven cavity, Theoret. Comput. Fluid Dyn. 29 (2015) 245–261.
[34] A. Roma, C.S. Peskin, M.J. Berger, An adaptive version of the immersed boundary method, J. Comput. Phys. 153 (1999) 509–534.
[35] T. Kempe, J. Fröhlich, An improved immersed boundary method with direct forcing for the simulation of particle laden flows, J. Comput. Phys. 231 (2012) 3663–3684.
[36] K. Taira, T. Colonius, The immersed boundary method: A projection approach, J. Comput. Phys. 225 (2007) 3121–3133.
[37] Y. Feldman, Y. Gulbeg, An extension of the immersed boundary method based on the distributed Lagrange multiplier approach, J. Comput. Phys. 322 (2016) 248–266.
[38] M. Uhlmann, An immersed boundary method with direct forcing for the simulation of particulate flows, J. Comput. Phys. 209 (2005) 448–476.
[39] B.D. Hassard, N.D. Kazarinoff, Y.-H. Wan, Theory and Applications of Hopf Bifurcation, Mathematics Society Lecture Note Series, vol. 41, Mathematics Society, London, 1981.
[40] J. Jeong, F. Hussain, On the identification of a vortex, J. Fluid Mech. 285 (1995) 69–94.
[41] Y.A. Kuznetsov, Elements of Applied Bifurxation Theory, Applied Mathematical Sciences, second ed., vol. 112, Springer, 1998, pp. 273–288..